

Design of innovative self-expandable femoral stents using inverse  
homogenization topology optimization

*Original*

Design of innovative self-expandable femoral stents using inverse  
homogenization topology optimization / Carbonaro, Dario; Mezzadri, Francesco; Ferro, Nicola; DE NISCO, Giuseppe;  
Audenino, Alberto; Gallo, Diego; Chiastra, Claudio; Morbiducci, Umberto; Perotto., Simona. - In: COMPUTER  
METHODS IN APPLIED MECHANICS AND ENGINEERING. - ISSN 0045-7825. - ELETTRONICO. - (2023).  
[10.1016/j.cma.2023.116288]

*Availability:*

This version is available at: 11583/2980793 since: 2023-07-31T09:28:09Z

*Publisher:*

Elsevier

*Published*

DOI:10.1016/j.cma.2023.116288

*Terms of use:*

This article is made available under terms and conditions as specified in the corresponding bibliographic description in  
the repository

*Publisher copyright*

(Article begins on next page)

# Design of innovative self-expandable femoral stents using inverse homogenization topology optimization

Dario Carbonaro<sup>a,1</sup>, Francesco Mezzadri<sup>b,1</sup>, Nicola Ferro<sup>c,\*</sup>, Giuseppe De Nisco<sup>a</sup>,  
Alberto Luigi Audenino<sup>a</sup>, Diego Gallo<sup>a</sup>, Claudio Chiastra<sup>a</sup>, Umberto Morbiducci<sup>a</sup>,  
Simona Perotto<sup>c</sup>

<sup>a</sup> PoliTo<sup>BIO</sup> Med Lab, Department of Mechanical and Aerospace Engineering, Politecnico di Torino, Viale Duca degli Abruzzi, 24, Torino, Italy

<sup>b</sup> Department of Engineering Enzo Ferrari, University of Modena and Reggio Emilia, Via P. Vivarelli, 10/1, Modena, Italy

<sup>c</sup> MOX, Department of Mathematics, Politecnico di Milano, Piazza L. da Vinci, 32, Milano, Italy

Received 22 March 2023; received in revised form 20 June 2023; accepted 16 July 2023

Available online 8 August 2023

## Abstract

In this study, we propose a novel computational framework for designing innovative self-expandable femoral stents. First, a two-dimensional stent unit cell is designed by inverse homogenization topology optimization. In particular, the unit cell is optimized in terms of contact area with the target of matching prescribed mechanical properties. The topology optimization is enriched by an anisotropic mesh adaptation strategy, enabling a time- and cost-effective procedure that promotes original layouts. Successively, the optimized stent unit cell is periodically repeated on a hollow cylindrical surface to construct the corresponding three-dimensional device. Finally, structural mechanics and computational fluid dynamics simulations are carried out to verify the performance of the newly-designed stent. The proposed workflow is being tested through the design of five proof-of-concept stents. These devices are compared through specific performance evaluations, which include the assessments of the minimum requirement for usability, namely the ability to be crimped into a catheter, and the quantification of the radial force, the foreshortening, the structural integrity and the induced blood flow disturbances.

© 2023 The Author(s). Published by Elsevier B.V. This is an open access article under the CC BY-NC-ND license (<http://creativecommons.org/licenses/by-nc-nd/4.0/>).

**Keywords:** Peripheral artery disease; Nitinol stent; Topology optimization; Homogenization; Anisotropic adapted mesh; Computational fluid dynamics

## 1. Introduction

Vascular stents are minimally invasive mechanical devices designed as cylinder-like hollow structures obtained, in general, by the periodic repetition of a unit cell. Stent devices are deployed inside diseased blood vessels for providing mural support and preventing vessel obstruction after intervention. Depending on the treated pathology and implantation site, stents are available with different shapes, sizes and materials (mainly metallic), and have a narrow profile in a crimped (i.e., radially compressed) state to easily pass and be placed inside the vessels [1–4]. Vascular

\* Corresponding author.

E-mail address: [nicola.ferro@polimi.it](mailto:nicola.ferro@polimi.it) (N. Ferro).

<sup>1</sup> The two authors have equally contributed to the study.

## Nomenclature

<b>BAMG</b>	Bidimensional Anisotropic Mesh Generator
<b>CFD</b>	Computational Fluid-Dynamics
<b>FE</b>	Finite Element
<b>IPOPT</b>	Interior Point OPTimizer
<b>ISR</b>	In-Stent Restenosis
<b>NiTi</b>	Nickel-Titanium
<b>SIMPATY</b>	SIMP with AdaptivITy
<b>SIMP</b>	Solid Isotropic Material with Penalization
<b>TAWSS</b>	Time-Averaged Wall Shear Stress
<b>TO</b>	Topology Optimization
<b>TSVI</b>	Topological Shear Variation Index
<b>WSS</b>	Wall Shear Stress

stents are commonly divided into two major categories depending upon the deployment procedure [5]: balloon-expandable stents, usually made of stainless-steel, cobalt or platinum chromium alloy, which are manufactured in a crimped state and are plastically expanded to the vessel wall by balloon inflation; self-expandable stents, typically made of super-elastic Nickel-Titanium (NiTi), which are manufactured slightly oversized above the vessel diameter and elastically resume their initial shape after being crimped and released from the catheter, without the need for balloon inflation [1,6].

Whether it is a balloon- or a self-expandable device, stents may lead to well-established clinical issues, such as in-stent restenosis (ISR) (i.e., gradual vessel lumen re-narrowing caused by abnormal neointimal proliferation) and stent thrombosis (i.e., sudden occlusion of the vessel due to the formation of a blood clot), which represent two of the major complications still limiting the safety and success of stenting [7–9]. It has been verified that the geometric features of the stent unit cells may have a direct impact on the occurrence of ISR and stent thrombosis and, more in general, on the mechanical performance of the devices as well as on the clinical outcome of the treatment [3,4,8,10–13].

Over the last decades, significant research efforts have been conducted to improve the design of the stent unit cells for the obtainment of an adequate response of the device. Within this context, computational methods have been used as an efficient tool to virtually characterize and optimize the stent design, with great advantages in terms of associated costs. In recent years, *in silico* models have gained increasing momentum in the medical device industry, and structural mechanics simulations are commonly adopted to support the design process of stents, especially in the initial proof-of-concept stage [14,15]. For instance, several computational frameworks, merging geometric- with physics-based features, have been developed to optimize the mechanical performance of stents with the final goal of improving the effectiveness of the endovascular treatment [16–24].

Among the optimization strategies that can be used to aid the design of vascular stents, topology optimization (TO) represents an attractive procedure for the systematic design of new layouts of the devices. The idea is to optimize the topology of the stent in order to match specific design requirements [25]. Few contributions are available in the literature where a TO-based strategy is applied to vascular stent design. As possible examples, TO-based approaches have been applied to: a commercially available drug-eluting stent, aiming at increasing the stent strut stiffness while retaining the drug holding capacity [26]; the optimization of the stent material layout, tailoring the structure to achieve a bi-stable snap-through behavior [27]; the investigation of the material distribution of coronary artery auxetic stents, improving both the structural and hemodynamic properties of the device [28,29]; maximizing the radial stiffness of a polymeric stent [30].

In this work, we propose a computational framework based on TO for the design of innovative self-expandable femoral stents to be deployed inside diseased femoropopliteal arteries. This task is particularly challenging due to the severe deformations that femoropopliteal arteries undergo during lower limb movements [31,32], which in turn impose complex loading conditions to the implanted devices, leading to high failure rates [7]. The computational framework here presented is inspired by inverse homogenization, namely a consolidated technique for the optimal

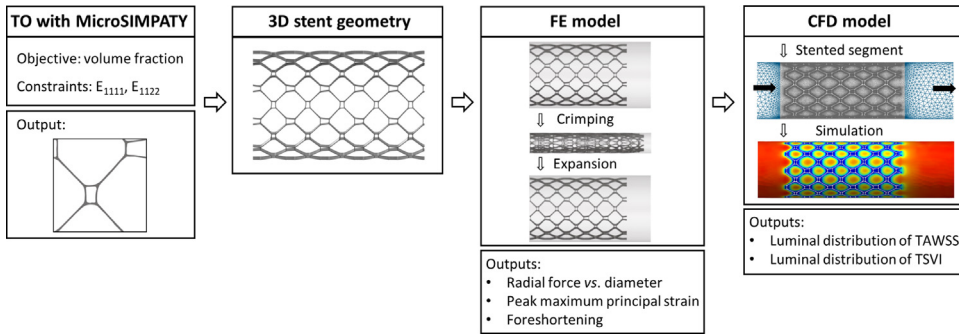


**Fig. 1.** Main steps of the workflow for the design and verification of new self-expandable femoral artery stents.

design of microscopic unit cells that confer desired properties to a lattice material at the macroscale [25]. Thus, since a stent can be conceived as the repetition of a unit cell onto a cylindrical surface, we aim to design from scratch new stent unit cells to ideally guarantee geometric, structural or hemodynamic properties to the whole device. With this aim, we resort to the microSIMPATY algorithm [33] which enhances a standard inverse homogenization topology optimization approach with a customized choice of the computational mesh in a finite element setting. In more detail, an anisotropic adapted mesh is adopted to make the design process time- and cost-effective through a fully automatic procedure. This phase constitutes the first step of a new design workflow that sequentially generates two-dimensional stent unit cells, periodically repeats the optimized cells on a hollow cylindrical surface for generating the three-dimensional stent design, and, finally, verifies the response of the device in terms of structural mechanics and computational fluid dynamics criteria.

The paper is organized as follows. Section 2 represents the modeling and methodological core of the manuscript, by setting the workflow yielding the new stent designs. In particular, after listing the stent design requirement and the assessment criteria under consideration in this work, in Section 2.1 we formalize the inverse homogenization TO procedure, with an example of an innovative 2D cell. Section 2.2 deals with the generation of a 3D stent, starting from the optimized unit layout. Sections 2.3 and 2.4 describe the structural mechanics and CFD analysis performed on the new stent designs. Section 3 is devoted to the numerical assessment of the whole pipeline on five proof-of-concept cell layouts. Section 4 discusses the obtained results, the limitations of the proposed methodology and some hints on possible future perspectives. Finally, Section 5 gathers concluding remarks.

## 2. Methods

The proposed procedure for the design of self-expandable femoral artery stents has the goal of delivering innovative devices that comply with standard regulations for vascular clinical practices, such as the minimization of the risks associated with the implantation. To this aim, we settle a workflow which consists of the steps: (i) inverse TO to generate 2D designs of stent unit cells meeting specific requirements (see Section 2.1); (ii) use of the identified 2D unit cells as the basis for generating 3D stent models (see Section 2.2); (iii) finite element (FE)-based simulations of the complete crimping cycle of the 3D stent models generated in (ii), in order to evaluate the nonlinear structural behavior (see Section 2.3); (iv) computational fluid dynamics (CFD) simulations on the generated 3D stent models in idealized vessels to assess the stent impact on the hemodynamics (see Section 2.4).

Fig. 1 shows the 2D–3D workflow, from the design to the verification of new self-expandable femoral artery stents. In particular, the design phase (i) aims at minimizing the contact area (i.e., the device volume fraction) between the stent and the luminal surface of the vessel, which, in turn, reduces the risks associated with tissue ingrowth, ISR and thrombosis [34,35]. The 2D–3D paradigm in phase (ii) is based on two main assumptions, consistently with the available literature [27,36]. First, the large mismatch between the stent strut thickness (200  $\mu\text{m}$ ) and the device cylindrical surface diameter (7 mm) justifies the employment of a plane stress setting in the design phase (i). In addition, we set a fixed strut thickness during the optimization process, since this is a distinguishing feature for femoral artery stents. As an advantageous byproduct, the employment of the 2D–3D framework reduces the computational cost of the design phase, with respect to a full 3D scenario. A posteriori, in the validation phases (iii) and (iv), we assess the biomechanical behavior of the femoral stent, by focusing on:

- the radial force applied by the implanted stent to the vessel wall, that has to be adequate for scaffolding the diseased artery, thus avoiding the damaging of the surrounding arterial wall tissue [3,37,38];
- the foreshortening of the stent, that enables a precise placement (i.e., covering the whole length of the lesion) once expanded in situ [3,37,38];
- the structural integrity of the stent, which is guaranteed by low (peak) maximum principal strains on the stent when encased inside the delivery system [18];
- the blood flow disturbances induced by the struts of the implanted stent, which are expected to be minimal, in order to reduce the risk factors promoting ISR or thrombosis [34].

## 2.1. The design of unit stent cells

The design of 2D stent unit cells – namely the first step of the workflow in Fig. 1 – has the principal goal of minimizing the contact area of the stent, jointly with the enforcement of suitable constraints on the stiffness of the stent unit cells, under prescribed loading conditions. With this aim, we adopt the microSIMPATY algorithm [33], which allows designing from scratch unit cells targeting prescribed properties through a TO process. Physical background and technical details of the microSIMPATY tool are provided in the two following sections and successively applied to a benchmark configuration in Section 2.1.3.

### 2.1.1. The physical background and the design strategy

MicroSIMPATY combines a standard topology optimization approach with the homogenization theory, and resorts to an anisotropic mesh adaptation procedure to increase the computational efficiency of the whole design algorithm. Hereafter, we formalize the reference physical framework, the selected topology optimization method, and the discretization scheme based on adapted meshes.

*The homogenization theory.* The physical setting that we adopt to design stent unit cells is represented by the homogenized linear elasticity model [39,40]. Homogenization is the standard mathematical process used to incorporate the information associated with the small scales (the stent unit cell, in the case under study) into a macroscopic problem (the whole stent). By resorting to an asymptotic expansion, it is customary to express the material properties by means of a single quantity,  $\mathbf{E}^H \in \mathbb{R}^{3 \times 3}$ , which replaces the stiffness tensor  $\mathbf{E} \in \mathbb{R}^{3 \times 3}$  in the linear constitutive stress–strain relation  $\boldsymbol{\sigma}(\mathbf{u}) = \mathbf{E}\boldsymbol{\varepsilon}(\mathbf{u})$ , with  $\mathbf{u}$  the displacement,

$$\boldsymbol{\sigma}(\mathbf{u}) = \begin{pmatrix} \sigma_{11}(\mathbf{u}) \\ \sigma_{22}(\mathbf{u}) \\ \sigma_{12}(\mathbf{u}) \end{pmatrix}, \quad \boldsymbol{\varepsilon}(\mathbf{u}) = \begin{pmatrix} \varepsilon_{11}(\mathbf{u}) \\ \varepsilon_{22}(\mathbf{u}) \\ 2\varepsilon_{12}(\mathbf{u}) \end{pmatrix}, \quad \mathbf{E} = \begin{pmatrix} E_{1111} & E_{1122} & E_{1112} \\ E_{2211} & E_{2222} & E_{2212} \\ E_{1211} & E_{1222} & E_{1212} \end{pmatrix}, \quad (1)$$

where  $\boldsymbol{\varepsilon}$  denotes the strain tensor  $(\nabla \mathbf{u} + \nabla \mathbf{u}^T)/2$  according to the Voigt notation [41]. Thus, we end up with the homogenized constitutive stress–strain relation  $\boldsymbol{\sigma}^H(\mathbf{u}) = \mathbf{E}^H \boldsymbol{\varepsilon}(\mathbf{u})$ , where the stiffness tensor  $\mathbf{E}^H$  can be expressed componentwise by

$$E_{ijkl}^H(\mathbf{u}^{*,ij}, \mathbf{u}^{*,kl}) = \frac{1}{|\Omega|} \int_{\Omega} [\boldsymbol{\sigma}(\mathbf{u}^{0,ij}) - \boldsymbol{\sigma}(\mathbf{u}^{*,ij})] : [\boldsymbol{\varepsilon}(\mathbf{u}^{0,kl}) - \boldsymbol{\varepsilon}(\mathbf{u}^{*,kl})] d\Omega, \quad (2)$$

where  $\Omega \subset \mathbb{R}^2$  denotes the unit cell of the stent, while  $\mathbf{u}^{*,mn}$  are the fluctuations induced by the test displacement fields  $\mathbf{u}^{0,mn}$ , for  $mn = ij, kl \in \mathcal{I} = \{11, 22, 12\}$ , with  $\mathbf{u}^{0,11} = (x_1, 0)^T$ ,  $\mathbf{u}^{0,22} = (0, x_2)^T$ ,  $\mathbf{u}^{0,12} = (x_2, 0)^T$ . Fluctuations  $\mathbf{u}^{*,mn}$  belong to a function space  $V$  to be properly selected and satisfy the equation

$$\int_{\Omega} \boldsymbol{\sigma}(\mathbf{u}^{*,mn}) : \boldsymbol{\varepsilon}(\mathbf{v}) d\Omega = \int_{\Omega} \boldsymbol{\sigma}(\mathbf{u}^{0,mn}) : \boldsymbol{\varepsilon}(\mathbf{v}) d\Omega \quad \forall \mathbf{v} \in V. \quad (3)$$

The state equation (3) is solved in the space  $V = [H_{\odot}^1(\Omega)]^2$  of the  $H^1(\Omega)$ -vector functions<sup>2</sup> satisfying periodic boundary conditions along the cell boundary,  $\partial\Omega$ , according to the asymptotic homogenization theory.

<sup>2</sup> Throughout the paper, we adopt standard notations for the function spaces following [42].

*Inverse homogenization topology optimization.* TO searches the optimal distribution of a material inside a design domain,  $\Omega$ , targeting prescribed objectives under a set of physical and design constraints. In such a context, it is customary to model the distribution of the material in  $\Omega$  by means of a function,  $\mathbf{1}_{\Omega^{mat}}$ , which indicates the portions of the domain where the material is present or not, being

$$\mathbf{1}_{\Omega^{mat}}(\mathbf{x}) = \begin{cases} 1 & \text{for } \mathbf{x} = (x_1, x_2) \in \Omega^{mat} \\ 0 & \text{for } \mathbf{x} = (x_1, x_2) \in \Omega \setminus \Omega^{mat}, \end{cases} \quad (4)$$

with  $\Omega^{mat}$  the subset of material points in  $\Omega$ . The indicator function  $\mathbf{1}_{\Omega^{mat}}$  allows to generalize the constant stiffness tensor in (1) to a quantity varying in  $\Omega$ , so that  $\mathbf{E}$  is replaced by

$$\mathbf{E}_1(\mathbf{x}) = \mathbf{1}_{\Omega^{mat}}(\mathbf{x})\mathbf{E}^0, \quad (5)$$

with  $\mathbf{E}^0 \in \mathbb{R}^{3 \times 3}$  the stiffness tensor of the selected isotropic material. The indicator function assigns non-zero stiffness values only to the portion of the domain occupied by material, the full-material configuration in (1) being recovered for  $\Omega^{mat} \equiv \Omega$ .

From a computational viewpoint, function  $\mathbf{1}_{\Omega^{mat}}(\mathbf{x})$  enables the solution of the problem of interest to the material domain  $\Omega^{mat}$ , while setting the equations in the whole design domain  $\Omega$ . In practice, the Boolean function  $\mathbf{1}_{\Omega^{mat}}$  is regularized, for instance, by resorting to a level set function [43], or by introducing a continuous auxiliary function  $\rho$ , which models the density material distribution inside the design domain  $\Omega$  [25]. In this work, we adopt the latter approach. In particular, function  $\rho$  takes values in  $[0, 1]$ , where  $\rho(\mathbf{x}) = 1$  identifies solid material points, while  $\rho(\mathbf{x}) = 0$  corresponds to void. Vice versa, intermediate density values ( $0 < \rho(\mathbf{x}) < 1$ ) correspond to a non-physical material state. In order to limit the presence of such intermediate densities, we resort to the well-known Solid Isotropic Material with Penalization (SIMP) approach [25], which leads us to replace the stiffness tensor in (5) with

$$\mathbf{E}_\rho(\mathbf{x}) = \rho^p(\mathbf{x})\mathbf{E}^0, \quad (6)$$

where  $p > 0$  is a penalization exponent.

Thus, a generic SIMP-based TO approach can be stated as the following constrained minimization problem:

$$\min_{\rho} J(\mathbf{w}(\rho), \rho) \quad : \quad \begin{cases} a_{\rho}(\mathbf{w}(\rho), \mathbf{v}) = f_{\rho}(\mathbf{v}) \quad \forall \mathbf{v} \in \mathcal{V} \\ \underline{\mathbf{c}} \leq \mathbf{c}(\mathbf{w}(\rho), \rho) \leq \bar{\mathbf{c}} \\ \underline{\rho} \leq \rho \leq 1, \end{cases} \quad (7)$$

where  $J(\cdot, \rho)$  is the objective functional; the first constraint models the physics underlying the minimization process, with  $\mathbf{w}$  and  $\mathbf{v}$  the trial and the test function in  $\mathcal{V}$ , respectively; the second constraint introduces a lower and an upper control ( $\underline{\mathbf{c}}$  and  $\bar{\mathbf{c}}$ , respectively) onto the physical and/or design quantities collected in  $\mathbf{c}(\cdot, \rho)$ ; the third inequality imposes an admissible range for  $\rho$ , the null value being replaced by  $\underline{\rho} > 0$  to avoid numerical drawbacks. In general, TO problem (7) is non-convex, and the uniqueness of the minimum can be ensured only by introducing a sufficient number of constraints.

As regards the TO problem applied to the design of stents, we particularize problem (7) as

$$\min_{\rho} J_S(\mathbf{u}^*(\rho), \rho) \quad : \quad \begin{cases} a_{\rho}^{ij}(\mathbf{u}^{*,ij}(\rho), \mathbf{v}) = f_{\rho}^{ij}(\mathbf{v}) \quad \forall \mathbf{v} \in \mathcal{V}, \quad ij \in \mathcal{I} \\ \underline{\mathbf{e}}_C \leq \mathbf{e}_{C,\rho}^H(\mathbf{u}^*(\rho)) \leq \bar{\mathbf{e}}_C \\ \underline{\rho} \leq \rho \leq 1, \end{cases} \quad (8)$$

where  $\mathbf{u}^*(\rho)$  collects the fluctuation displacement components  $\mathbf{u}^{*,ij}(\rho)$  in (3);  $\mathbf{e}_{C,\rho}^H(\mathbf{u}^*(\rho))$  gathers the homogenized stiffness tensor components

$$\mathbf{E}_{qrst,\rho}^H(\mathbf{u}^{*,qr}, \mathbf{u}^{*,st}) = \frac{1}{|\Omega|} \int_{\Omega} \rho^p [\boldsymbol{\sigma}(\mathbf{u}^{0,qr}) - \boldsymbol{\sigma}(\mathbf{u}^{*,qr})] : [\boldsymbol{\varepsilon}(\mathbf{u}^{0,st}) - \boldsymbol{\varepsilon}(\mathbf{u}^{*,st})] d\Omega,$$

constraining the design process, with  $qrst \in \mathcal{I}^* \subseteq \{ijkl : ij, kl \in \mathcal{I}\}$ , and where the dependence of  $\mathbf{u}^{*,ij}(\rho)$  on  $\rho$  has been dropped to simplify the notation; vectors  $\underline{\mathbf{e}}_C$  and  $\bar{\mathbf{e}}_C$  provide the lower and upper bounds associated with the components  $\mathbf{E}_{qrst,\rho}^H$ , which are expected to be compatible with the theoretical Hashin–Shtrikman bounds [44].

Since we are interested in controlling the contact area between the stent and the luminal surface of the vessel, we select the goal functional in (8) as the quadratic deviation between a target volume fraction,  $V_f$ , and the actual

volume of the structure, namely

$$J_S(\mathbf{u}^*, \rho) = J_S(\rho) = \left( \frac{1}{|\Omega|} \int_{\Omega} \rho d\Omega - V_f \right)^2. \quad (9)$$

In particular, minimizing the volume of the stent unit cell leads to choose  $V_f = 0$  in (9) so that  $J_S(\rho)$  simplifies to  $|\Omega|^{-1} \int_{\Omega} \rho d\Omega$ .

The physical model constraining the TO in (8) coincides with the SIMP-variant of Eq. (3) for the displacement fluctuations in the unit cell, being

$$\begin{aligned} a_{\rho}^{ij}(\mathbf{u}^{*,ij}, \mathbf{v}) &= \int_{\Omega} \rho^p \boldsymbol{\sigma}(\mathbf{u}^{*,ij}) : \boldsymbol{\varepsilon}(\mathbf{v}) d\Omega, \\ f_{\rho}^{ij}(\mathbf{v}) &= \int_{\Omega} \rho^p \boldsymbol{\sigma}(\mathbf{u}^{0,ij}) : \boldsymbol{\varepsilon}(\mathbf{v}) d\Omega, \end{aligned} \quad (10)$$

with  $\mathcal{V} = V = [H_{\odot}^1(\Omega)]^2$ .

With a view to the discretization of the optimization problem (8), we resort to a FE approximation for the design variable  $\rho$ , the displacement trial and the test functions,  $\mathbf{u}^{*,ij}$  and  $\mathbf{v}$ . We partition the stent unit cell design domain  $\Omega$  with a family of conforming tessellations  $\{\mathcal{T}_h\}_h$ , consisting of triangular elements  $K$  with  $h$  the maximum of the diameters  $h_K$ . In particular, here the discrete space selected for  $\rho$  coincides with the set of the  $\Omega$ -periodic piecewise affine polynomials,  $R_h = \{r_h \in C^0(\overline{\Omega}) : r_h|_K \in \mathbb{P}_1(K)\} \cap H_{\odot}^1(\Omega)$ , while the components  $\mathbf{u}^{*,ij}$  of  $\mathbf{u}^*$  and  $\mathbf{v}$  are chosen in  $V_h = [R_h]^2$ , so that the discrete counterpart of (8) can be expressed as

$$\min_{\rho_h} J_S(\rho_h) \quad : \quad \begin{cases} a_{\rho_h}^{ij}(\mathbf{u}_h^{*,ij}, \mathbf{v}_h) = f_{\rho_h}^{ij}(\mathbf{v}_h) & \forall \mathbf{v}_h \in V_h, \quad ij \in \mathcal{I} \\ \underline{\mathbf{e}}_C \leq \mathbf{e}_{C,\rho_h}^H(\mathbf{u}_h^*) \leq \overline{\mathbf{e}}_C \\ \rho \leq \rho_h \leq 1. \end{cases} \quad (11)$$

**Anisotropic adaptive finite element discretization.** To manage the discrete constrained optimization problem in (11), we adopt the recently proposed microSIMPATY algorithm [33], which combines SIMP inverse homogenization with an anisotropic mesh adaptation strategy. This approach allows overcoming some of the limitations hampering the use of the discrete SIMP formulation, in particular the ones related to the adopted approximation, such as the greyscale effect, the generation of jagged boundaries as well as of complex structures which are far from being manufacturable [45,25]. Moreover, the use of an adaptive mesh ensures to limit the employment of filtering techniques in the design and the post-processing of the optimized layout, thus yielding an automatic and cost-effective tool.

Anisotropic adapted meshes are recognized as an ideal instrument to model problems characterized by strong gradients along certain directions. This is the case of the design of structures where the material density exhibits a sharp gradient along the solid/void interface. The benefits led by the employment of a customized mesh within the TO process have been widely investigated for applications both at the macro- and at the micro-scale [46–52].

The key role played by the gradient of the density function in the topology optimization of structures suggested selecting  $\nabla \rho$  as a driving quantity for the adaptation of the computational mesh. With this aim, we adopt the well-known a posteriori recovery-based error estimator proposed by O.C. Zienkiewicz and J.Z. Zhu in [53,54] to control the  $H^1(\Omega)$ -seminorm of the discretization error. In the case of the optimization of structures, we apply such an estimator to the density function. This leads us to replace the seminorm

$$|e_h(\rho)|_{H^1(\Omega)} = \left[ \int_{\Omega} |\nabla \rho - \nabla \rho_h|^2 d\Omega \right]^{1/2} = \left[ \sum_{K \in \mathcal{T}_h} \int_K |\nabla \rho - \nabla \rho_h|^2 dK \right]^{1/2} \quad (12)$$

with the computable value

$$\xi = \left[ \sum_{K \in \mathcal{T}_h} \xi_K^2 \right]^{1/2} = \left[ \sum_{K \in \mathcal{T}_h} \int_K |\boldsymbol{\Xi}_P(\rho_h)|^2 dK \right]^{1/2}, \quad (13)$$

$\boldsymbol{\Xi}_P(\rho_h) = \mathbf{P}(\rho_h) - \nabla \rho_h$  being the recovered error. Quantities  $\xi$  and  $\xi_K$  denote the global and local error estimator;  $\mathbf{P}(\rho_h)$  represents the so-called recovered gradient which surrogates the exact (unknown) gradient  $\nabla \rho$  in (12), by averaging and/or projecting the discrete gradient  $\nabla \rho_h$ . Several recipes are available in the literature to define

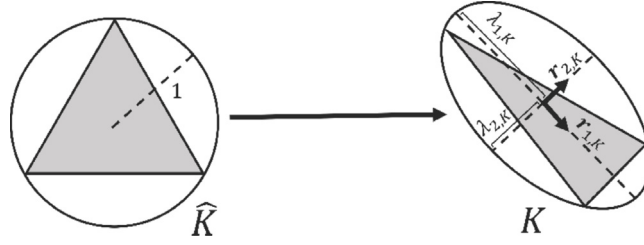


Fig. 2. Sketch of the main quantities defining the anisotropy of element  $K$ .

$\mathbf{P}(\rho_h)$  [54–59]. MicroSIMPATY employs the recovery formula

$$\mathbf{P}(\rho_h)(\mathbf{x}) = [P_1(\rho_h)(\mathbf{x}), P_2(\rho_h)(\mathbf{x})]^T = |\Delta_K|^{-1} \sum_{T \in \Delta_K} |T| \nabla \rho_h|_T(\mathbf{x}) \quad \mathbf{x} \in K, \quad (14)$$

with  $\Delta_K = \{T \in \mathcal{T}_h : T \cap K \neq \emptyset\}$  the patch of elements associated with  $K$ , and  $|\Delta_K|$  the patch area. Recipe (14), coinciding with an area-weighted average of the discrete gradient across the elements in  $\Delta_K$ , is here selected since it is straightforward to be computed, cost-effective, and it turns out to be instrumental to an easy generalization of estimator (13) to an anisotropic setting. Indeed, following [60], we consider the anisotropic counterpart of estimator  $\xi$ , given by

$$\eta = \left[ \sum_{K \in \mathcal{T}_h} \eta_K^2 \right]^{1/2},$$

with

$$\eta_K^2 = \frac{1}{\lambda_{1,K} \lambda_{2,K}} \sum_{i=1}^2 \lambda_{i,K}^2 (\mathbf{r}_{i,K}^T \mathbf{G}_{\Delta_K}(\Xi_P(\rho_h)) \mathbf{r}_{i,K}). \quad (15)$$

In (15) the quantities  $\lambda_{i,K}$  (with  $\lambda_{1,K} \geq \lambda_{2,K} > 0$ ) and  $\mathbf{r}_{i,K}$ ,  $i = 1, 2$ , fully characterize size, shape and orientation of the generic element  $K$ , providing the length and the direction of the semi-axes of the ellipse circumscribed to  $K$  (see Fig. 2). Furthermore, the symmetric positive semidefinite matrix  $\mathbf{G}_{\Delta_K}$ , with entries

$$[\mathbf{G}_{\Delta_K}(\Xi_P(\rho_h))]_{ij} = \sum_{T \in \Delta_K} \int_T \Xi_{P,i}(\rho_h) \Xi_{P,j}(\rho_h) dT \quad i, j = 1, 2, \quad (16)$$

separates the components  $\Xi_{P,k}(\rho_h) = P_k(\rho_h) - \partial_{x_k} \rho_h \in L^2(\Omega)$  ( $k = 1, 2$ ) of the recovered error, in order to be projected along the anisotropic directions. Finally, the scaling factor  $(\lambda_{1,K} \lambda_{2,K})^{-1}$  guarantees the consistency of the anisotropic estimator  $\eta$  with the isotropic case in (13).

To exploit the estimator in (15) for the generation of an anisotropic adapted mesh which captures the steep gradients characterizing  $\rho_h$ , we follow the metric-based approach in [61]. This technique allows us to predict the new local geometric features,  $\mathcal{M}_K = \{\lambda_{i,K}^A, \mathbf{r}_{i,K}^A\}_{i=1,2}$  for each  $K \in \mathcal{T}_h$ , constituting the global metric  $\mathcal{M} = \{\mathcal{M}_K\}_{K \in \mathcal{T}_h}$  associated with the new adapted mesh. To define  $\mathcal{M}_K$ , we employ an optimization procedure based on the following criteria:

- (C1) setting of a user-defined accuracy,  $\text{tol}_\eta$ , onto the global estimator;
- (C2) minimization of the mesh cardinality  $\#\mathcal{T}_h$  (i.e., the number of the mesh elements);
- (C3) equidistribution of the tolerance  $\text{tol}_\eta$  throughout the mesh elements.

Criterion (C1) allows tuning the accuracy of the discrete solution according to the specific user's demands; the second rule implements a mesh cheapness requirement and is equivalent to maximize the area of each triangle; (C3) balances the estimator distribution across the new grid, imposing

$$\eta_K^2 = \frac{\text{tol}_\eta^2}{\#\mathcal{T}_h}. \quad (17)$$

To guarantee the minimization of the mesh cardinality, we rescale the local estimator in (15) with respect to the area of the patch, so that

$$\eta_K^2 = C_K \lambda_{1,K} \lambda_{2,K} \left[ s_K \left( \mathbf{r}_{1,K}^T \mathbf{G}_{\Delta_K}^* (\boldsymbol{\Xi}_P) \mathbf{r}_{1,K} \right) + \frac{1}{s_K} \left( \mathbf{r}_{2,K}^T \mathbf{G}_{\Delta_K}^* (\boldsymbol{\Xi}_P) \mathbf{r}_{2,K} \right) \right],$$

with  $C_K$  an explicitly computable constant,  $s_K = \lambda_{1,K}/\lambda_{2,K} \geq 1$  the aspect ratio of the element  $K$ , measuring the deformation of the triangle (with  $s_K = s_K^\Delta = 1$  corresponding to an equilateral triangle),  $\mathbf{G}_{\Delta_K}^* (\boldsymbol{\Xi}_P) = \mathbf{G}_{\Delta_K} (\boldsymbol{\Xi}_P)/|\Delta_K|$  the scaled counterpart of the matrix in (16). We observe that the dependence of the recovered error on  $\rho_h$  has been dropped.

The equivalence between the mesh cardinality minimization and the element area maximization, combined with equality (17), leads us to solve the following constrained minimization problem on each element  $K \in \mathcal{T}_h$ :

$$\min_{s_K, \mathbf{r}_{i,K}} \mathcal{I}_K(s_K, \{\mathbf{r}_{i,K}\}_{i=1,2}) : \begin{cases} \mathbf{r}_{i,K} \cdot \mathbf{r}_{j,K} = \delta_{ij} \\ s_K \geq 1, \end{cases} \quad (18)$$

with

$$\mathcal{I}_K(s_K, \{\mathbf{r}_{i,K}\}_{i=1,2}) = s_K \left( \mathbf{r}_{1,K}^T \mathbf{G}_{\Delta_K}^* (\boldsymbol{\Xi}_P) \mathbf{r}_{1,K} \right) + \frac{1}{s_K} \left( \mathbf{r}_{2,K}^T \mathbf{G}_{\Delta_K}^* (\boldsymbol{\Xi}_P) \mathbf{r}_{2,K} \right),$$

and  $\delta_{ij}$  the Kronecker symbol. Problem (18) admits an explicit solution  $\{s_K^A, \mathbf{r}_{i,K}^A\}_{i=1,2}$ , given by

$$s_K^A = \sqrt{g_{1,K}/g_{2,K}}, \quad \mathbf{r}_{1,K}^A = \mathbf{g}_{2,K}, \quad \mathbf{r}_{2,K}^A = \mathbf{g}_{1,K}, \quad (19)$$

where  $\{g_{i,K}, \mathbf{g}_{i,K}\}_{i=1,2}$  denote the eigenpairs associated with matrix  $\mathbf{G}_{\Delta_K}^* (\boldsymbol{\Xi}_P)$  [61]. Relation (17) is finally exploited to derive the two optimal anisotropic lengths  $\lambda_{1,K}^A$  and  $\lambda_{2,K}^A$  from the aspect ratio  $s_K^A$  in (19), thus obtaining

$$\lambda_{1,K}^A = g_{2,K}^{-1/2} \left( \frac{\text{tol}_\eta^2}{2\#\mathcal{T}_h C_K} \right)^{1/2}, \quad \lambda_{2,K}^A = g_{1,K}^{-1/2} \left( \frac{\text{tol}_\eta^2}{2\#\mathcal{T}_h C_K} \right)^{1/2}. \quad (20)$$

The optimal lengths  $\lambda_{i,K}^A$  in (20) and directions  $\mathbf{r}_{i,K}^A$  in (19) constitute the optimal metric  $\mathcal{M}_K$  associated with triangle  $K$ . These local metrics define the global metric  $\mathcal{M}$  to be passed as an input to a metric-based mesh generator, as detailed in the next section. The interested reader can find more insights about the whole adaptive process in [61].

### 2.1.2. MicroSIMPATY algorithm for the design of engineered stent unit cells

In this section, we focus on the main software tools used to implement microSIMPATY algorithm. Concerning the solution to problem (11), we resort to: FreeFEM [62] as a FE solver to approximate the state equations constraining the optimization process; the large-scale nonlinear Interior Point OPTimizer (IPOPT) [63] to carry out the constrained minimization; the mesh generator BAMG (Bidimensional Anisotropic Mesh Generator) integrated in FreeFEM to build the adapted mesh [64]. In particular, BAMG requires the metric  $\mathcal{M}$  at the vertices,  $\mathbf{z}$ , of the mesh  $\mathcal{T}_h$ . For this reason, we convert the piecewise constant metric,  $\mathcal{M} = \{\mathcal{M}_K\}$ , defined by (19)–(20) into a piecewise linear field,  $\tilde{\mathcal{M}} = \{\tilde{\mathcal{M}}_{\mathbf{z}}\}$ , by using the average

$$\tilde{\mathcal{M}}_{\mathbf{z}} = \frac{1}{|\Delta_{\mathbf{z}}|} \sum_{K \in \Delta_{\mathbf{z}}} |K| \mathcal{M}_K, \quad (21)$$

with  $\Delta_{\mathbf{z}}$  the patch of elements associated with vertex  $\mathbf{z}$ .

As a last step, we further improve metric  $\tilde{\mathcal{M}}$  in order to avoid any numerical bias in the structural mechanical analysis [65]. Indeed, it is known that elongated elements may influence the reliability of such an analysis, leading to an under-/over-estimation of the quantities involved in the design process. To overcome this issue, we adopt the strategy proposed in [66], where highly stretched triangles are alternated to isotropic elements of size  $h_{\text{iso}}$ . The idea is to exploit the capability of an anisotropic mesh of sharply tracking the layout boundaries, while preserving shape-regular triangles in the internal part of the structure to keep the computed mechanical quantities unbiased. We refer to such hybrid computational tessellation as to a graded mesh.

The overall design procedure supported by microSIMPATY is listed in Algorithm 1. The input parameters are: three tolerance values and a maximum number of iterations, constraining the design process; the bounds characterizing the box inequalities in (11) together with the set of indices  $\mathcal{I}^*$  identifying the homogenized stiffness tensor components for the design process; the goal volume fraction involved in the definition of functional  $J_S$  in (9);

the initial material density and mesh. The choice of the input parameters unavoidably affects the output layout  $\tau$ . In particular, the literature confirms the influence of the initial design setting on the final structure (see, e.g., [45]).

---

**Algorithm 1** microSIMPATY for engineered stent unit cells design

---

```

1: Input:  $\text{tol}_J, \text{tol}_\eta, \text{tol}_M, k_{\max}, \underline{\rho}, \underline{\mathbf{e}}_C, \bar{\mathbf{e}}_C, \mathcal{I}^*, V_f, \rho_h^{(0)}, \mathcal{T}_h^{(0)}$ 
2: Set  $k = 0, \text{err}_M = 1 + \text{tol}_M$ ;
3: while  $\text{err}_M > \text{tol}_M$  and  $k < k_{\max}$  do
4:    $\tilde{\rho}_h^{(k+1)} = \text{IPOPT}(\rho_h^{(k)}, \mathcal{T}_h^{(k)}, V_f, \underline{\rho}, \underline{\mathbf{e}}_C, \bar{\mathbf{e}}_C, \mathcal{I}^*, \mathcal{G}, \nabla_\rho \mathcal{G}, \text{tol}_J)$ ;
5:    $\rho_h^{(k+1)} = \text{filtering}(\tilde{\rho}_h^{(k+1)}, \beta, r_f)$ ;
6:    $\mathcal{T}_h^{(k+1)} = \text{adaptation}(\mathcal{T}_h^{(k)}, \rho_h^{(k+1)}, \text{tol}_\eta)$ ;
7:    $\text{err}_M = |\#\mathcal{T}_h^{(k+1)} - \#\mathcal{T}_h^{(k)}| / \#\mathcal{T}_h^{(k)}$ ;
8:    $k = k + 1$ 
9: end while
10:  $\tau = \rho_h^{(k)}$ ;
11:  $\mathbf{E}_\tau^H = \text{homogenize}(\tau)$ ;
12: Output:  $\tau, \mathbf{E}_\tau^H$ 

```

---

MicroSIMPATY alternates an optimization step (line 4), a filtering phase (line 5) and the anisotropic mesh adaptation procedure (line 6), within a **while** loop, controlled in terms of the stagnation of the relative mesh cardinality and of the maximum number,  $k_{\max}$ , of allowed iterations.

Function IPOPT returns the new density distribution  $\tilde{\rho}_h^{(k+1)}$  obtained starting from the current design variable  $\rho_h^{(k)}$  associated with mesh  $\mathcal{T}_h^{(k)}$ , in order to match tolerance  $\text{tol}_J$ . In particular, vector  $\mathcal{G}$  gathers the goal functional and the constrained quantities, namely,

$$\mathcal{G} = [J_S(\rho), \mathbf{e}_{C,\rho}^H]^T, \quad (22)$$

while  $\nabla_\rho \mathcal{G}$  collects the associated sensitivities (see [50] for more details, where a Lagrangian approach is adopted to compute the derivative of the components of  $\mathcal{G}$  with respect to  $\rho$ ).

Concerning the filtering phase, we employ a differentiable variant of the Heaviside function, characterized by parameter  $\beta$ , and a Helmholtz-like filter with a radius equal to  $r_f$  [67,68]. The action of the Heaviside function is to sharpen the layout boundary by removing the intermediate material densities (the larger  $\beta$ , the more clear-cut the boundary design). The Helmholtz-like filter smooths the irregularities and erases the thin features possibly arising along the structure boundary (the larger  $r_f$ , the more effective the smoothing action).

Successively, the filtered density  $\rho_h^{(k+1)}$  is used by function adaptation to compute the nodewise metric in (21) and to generate the new anisotropic adapted mesh.

MicroSIMPATY algorithm returns the optimized layout  $\tau$  together with the associated homogenized stiffness tensor  $\mathbf{E}_\tau^H$  of components

$$E_{ijkl,\tau}^H(\mathbf{u}^{*,ij}, \mathbf{u}^{*,kl}) = \frac{1}{|\Omega|} \int_{\Omega} \tau^p [\boldsymbol{\sigma}(\mathbf{u}^{0,ij}) - \boldsymbol{\sigma}(\mathbf{u}^{*,ij})] : [\boldsymbol{\epsilon}(\mathbf{u}^{0,kl}) - \boldsymbol{\epsilon}(\mathbf{u}^{*,kl})] d\Omega,$$

for  $ij, kl \in \mathcal{I}$ .

### 2.1.3. An example of innovative stent base cells

In this section, we investigate the performance of Algorithm 1 on a first case study, while referring to Section 3.1 for different optimization scenarios. We carry out the design phase in a non-dimensional setting to promote the generality of the framework, thus being fully independent of any specific material and cell dimension.

Concerning the physical background, we identify the design domain  $\Omega$  with the square  $(0, 10)^2$ . We consider an isotropic reference material with constitutive law  $\boldsymbol{\sigma}(\mathbf{u}) = 2\mu \boldsymbol{\epsilon}(\mathbf{u}) + \lambda \text{tr}(\boldsymbol{\epsilon}(\mathbf{u}))\mathbf{I}$ , being  $\lambda = E_Y \nu / [(1 + \nu)(1 - 2\nu)]$  and  $\mu = E_Y / [2(1 + \nu)]$  the Lamé coefficients,  $E_Y = 60$  and  $\nu = 0.33$  the Young modulus and the Poisson ratio,  $\text{tr}(\cdot)$  the trace operator, and  $\mathbf{I}$  the identity tensor. Finally, the SIMP penalization exponent  $p$  in (10) is set to 4.

The optimization in line 4 of Algorithm 1 is performed by setting  $\rho_h^{(0)} = |\sin(2\pi x/8) \sin(2\pi y/8)|$  on an initial structured grid,  $\mathcal{T}_h^{(0)}$ , with 5000 elements,  $V_f = 0$ ,  $\underline{\rho} = 10^{-4}$ ,  $\mathcal{I}^* = \{1111, 1122\}$ ,  $\underline{\mathbf{e}}_C = [\underline{E}_{1111}, \underline{E}_{1122}]^T =$

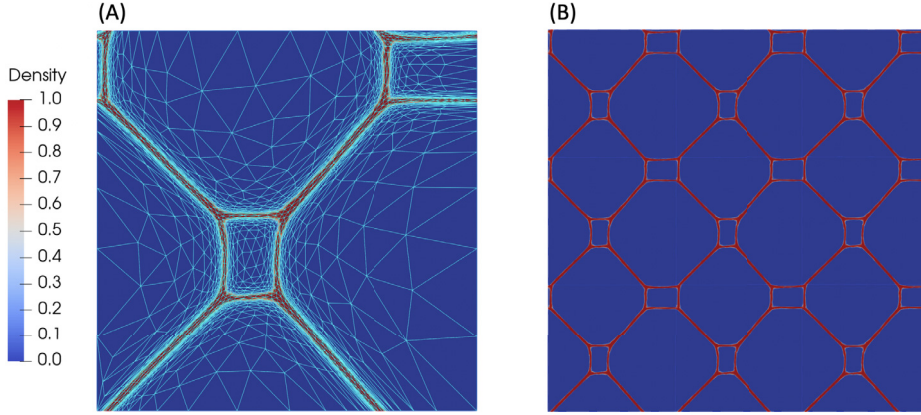


**Fig. 3.** Design 1. Optimized unit cell  $\tau$  and associated graded mesh (A);  $3 \times 3$  periodic lattice (B).

$[0.25, 0.50]^T$ ,  $\bar{\mathbf{e}}_c = [\bar{E}_{1111}, \bar{E}_{1122}]^T = [1.0, 1.0]^T$ ,  $\mathcal{G}$  as in (22) with  $\mathbf{e}_{c,\rho}^H = [E_{1111,\rho}^H, E_{1122,\rho}^H]^T$ , and  $\text{tol}_f = 10^{-6}$ . Function  $\rho_h^{(0)}$ , characterized by uniformly distributed circular holes, is expected to promote a feature-rich final optimized structure. Quantities  $E_{1111,\rho}^H$  and  $E_{1122,\rho}^H$  are here considered to generate the proof-of-concept design, although any other component of the homogenized stiffness tensor could be included in  $\mathbf{e}_{c,\rho}^H$ , according to the specific design requirement.

The filtering consists of a sharpening of the material/void interface, followed by a smoothing of the possible irregularities along such a boundary at each iteration. With this aim, the parameter of the Heaviside function is chosen as  $\beta = 2$ , while the filtering radius  $r_f$  for the Helmholtz filter is set to 0.06 and reduced by a factor of 1.5 at each iteration  $k$ .

The anisotropic mesh adaptation is tuned by the tolerance  $\text{tol}_\eta = 10^{-3}$ . Finally, the design iterations are controlled by parameters  $\text{tol}_M$  and  $k_{\max}$  selected equal to  $10^{-5}$  and 5, respectively.

MicroSIMPATY algorithm delivers the stent unit cell of Fig. 3, panel (A) (referred to as Design 1 in the sequel) after 5 iterations, completed in 395 seconds.<sup>3</sup> The output volume fraction is 6.11% of the initial design domain volume. This justifies the very thin struts and guarantees a low contact area in the final cell layout. The mesh adaptation procedure, graded with  $h_{\text{iso}} = 1/40$ , yields a final grid consisting of 12304 elements, whose maximum deformation is confined along the cell boundary and corresponds to  $s_K^{\max} = 60.11 \gg s_K^\Delta$ .

The homogenized stiffness tensor associated with Design 1 is

$$\mathbf{E}_\tau^H = \begin{pmatrix} 0.497 & 0.507 & 0.010 \\ 0.507 & 0.545 & 0.013 \\ 0.010 & 0.013 & 0.046 \end{pmatrix}, \quad (23)$$

which corroborates that the two box constraints in (11) are matched, approaching the lower bound in both cases.

Finally, we observe that the convergence history of the objective functional, of the box constraints, and of the mesh cardinality are very similar to the ones in [69, Fig. 3].

**Remark 1.** We assess the reliability of the graded mesh in accurately computing the mechanical properties, for a given fixed design layout. To this aim, we project the density field  $\tau$  in Fig. 3 onto: (1) a mesh characterized by 500 uniform subintervals along the cell sides, assumed as the ground truth (GT); (2) the mesh in Fig. 3 when varying the uniform diameter,  $h_{\text{iso}}$ , of the internal isotropic tessellation, while preserving the anisotropic elements along the design boundary. Successively, we evaluate the associated homogenized stiffness tensor, denoted by  $\mathbf{E}_{\tau,GT}^H$  and  $\mathbf{E}_{\tau,h_{\text{iso}}}^H$ , respectively.

<sup>3</sup> The computations have been run on a MacBook Pro laptop (2022), equipped with Apple M1-Pro CPU (2.064–3.228 GHz) and 32 GBs of RAM.

**Table 1**  
Reliability of the graded mesh in terms of mechanical properties for different values for  $h_{\text{iso}}$ .

$h_{\text{iso}}$	$\text{Err}_{2,h_{\text{iso}}}$	$\#\mathcal{T}_h$
1/20	9.33	8880
1/30	6.27	13530
1/40	5.50	12304
1/50	5.45	21260

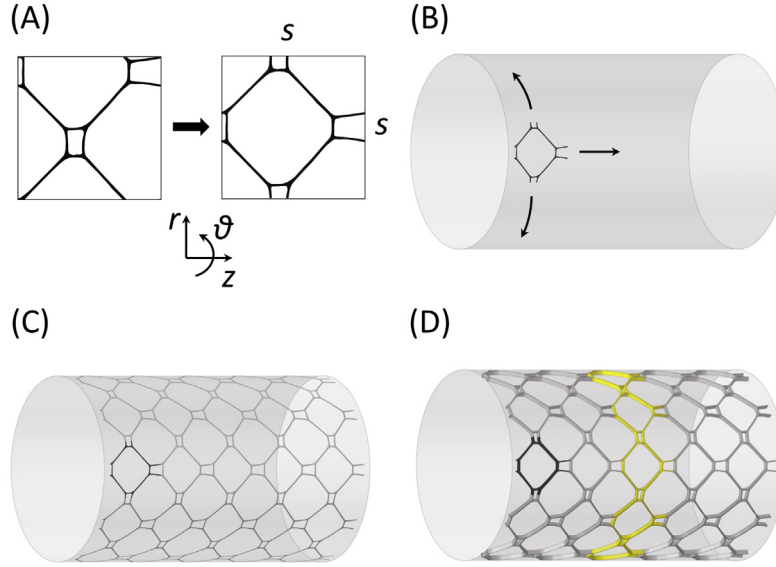


**Fig. 4.** 3D stent geometry reconstruction procedure: repositioning and scaling (A), projection (B), repetition (C), and extrusion (D). The adopted cylindrical coordinate reference system is highlighted in panel (A). For visualization clarity, only half stent is represented in panels (C) and (D).

We quantify the mismatch between  $\mathbf{E}_{\tau,h_{\text{iso}}}^H$  and  $\mathbf{E}_{\tau,GT}^H$  with respect to the 2-norm, by computing

$$\text{Err}_{2,h_{\text{iso}}} = \frac{\|\mathbf{E}_{\tau,h_{\text{iso}}}^H - \mathbf{E}_{\tau,GT}^H\|_2}{\|\mathbf{E}_{\tau,GT}^H\|_2} 100.$$

**Table 1** gathers the results of this reliability analysis, by providing the values of  $\text{Err}_{2,h_{\text{iso}}}$  and the mesh cardinality, for different choices of  $h_{\text{iso}}$ . We empirically observe that the percentage error decreases when  $h_{\text{iso}}$  approaches zero. This feature allows us to reach a prescribed accuracy provided that the internal isotropic tessellation is sufficiently fine, while preserving the computational benefits led by an anisotropic adapted mesh (e.g., for the design in [Fig. 3](#), 12304 elements of the graded mesh guarantee an accuracy similar to the one provided by the ground truth mesh consisting of 500000 elements).

## 2.2. 3D stent geometry reconstruction

This section focuses on the second block of the workflow of [Fig. 1](#) by describing how to obtain the 3D stent geometry from the 2D unit cell topologically optimized by microSIMPATY algorithm. In practice, we resort to a 4-step procedure implemented with Hypermesh software (Altair Engineering, Troy, MI, USA), which receives as input the .stl file of the optimized layout  $\tau$ . A dimensional notation for the material and domain size is adopted from this block onward, since, at this stage, the workflow moves from the abstract design phase to a practical stent performance analysis. The process is sketched in [Fig. 4](#) and consists in:

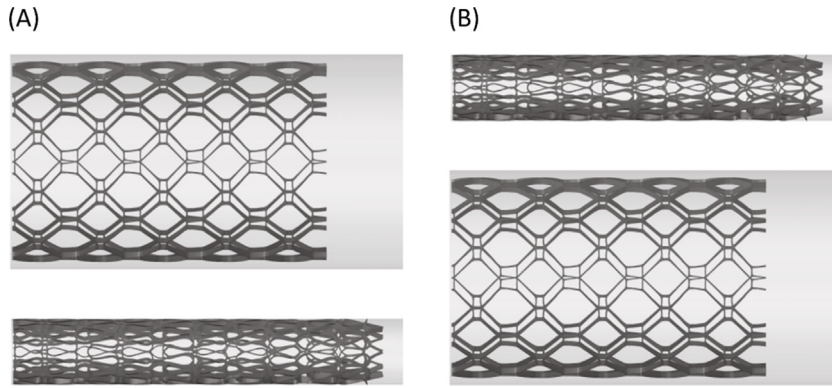


**Fig. 5.** FE structural analysis of a complete crimping cycle. (A) Crimping step. (B) Expansion step.

- the repositioning and the uniform scaling of the 2D unit cell by a factor  $s = \pi D/n$ , with  $D$  the diameter of the selected cylindrical surface and  $n$  the number of cell repetitions along the device circumference (panel (A)). This procedure is employed to avoid convergence issues of the nonlinear structural mechanics simulations of stent crimping;
- the projection of the 2D cell onto a cylindrical surface with diameter  $D = 7$  mm (panel (B));
- the repetition of the projected cell  $n = 10$  times along the circumferential ( $\theta$ ) and 5 times along the axial ( $z$ ) direction, respectively (panel (C)). The number of 5 unit cells repetition along the axial direction is selected to avoid undesirable boundary effects in the structural mechanics (see Section 2.3) and CFD simulations (see Section 2.4). Additionally, 10 repetitions along the circumferential direction are considered based on typical values reported in the literature for laser-cut stents [3,18,20,21];
- the extrusion of the surface lattice along the negative radial direction ( $r$ ), in order to assign a constant strut thickness equal to 0.2 mm (panel (D)), which is a typical value for commercially available femoral stents [36].

### 2.3. Structural response of the stent

The 2D unit cells yielded by microSIMPATY are generated under a linear elastic regime, without accounting for nonlinearities involving large deformations, buckling instability, super-elastic NiTi material behavior and contact conditions. However, in the third block of the workflow of Fig. 1, we carry out a nonlinear FE analysis of a complete crimping cycle to accurately characterize the structural performance of the new stent designs. Specifically, the crimping test is a standard method commonly performed to characterize the mechanical performance of stents [37,38], which aims to simulate the loading conditions that the stent experiences when it is inserted into a catheter and delivered to the deployment site.

To carry out this investigation, Hypermesh in conjunction with Abaqus/Standard (Dassault Systèmes Simulia Corp., Johnston, RI, USA) is used to implement the FE models. In particular, the structural FE simulations involve two components, namely the self-expandable NiTi stent and the crimping cylinder. The 3D stent geometry is discretized in Abaqus with C3D8R hexahedral elements with reduced integration, considering 4 and 10 elements across the strut width and thickness, respectively, according to previous computational studies [70,71]. The mechanical behavior of NiTi material is described by a super-elastic constitutive model [72], retrieving the material parameters from [73] and by assigning a constant body temperature of 37 °C. The crimping cylinder is modeled as a rigid cylindrical surface, with a diameter of 7.5 mm, and is discretized by using rigid surface elements SFM3D4R [74].

The structural FE analysis is carried out by using an implicit solver to deal with the nonlinear equations of static equilibrium, running on 6 computing cores of a workstation equipped with Intel® Core™ i7-8700 and 32 GB RAM. The analysis includes both the crimping and the expansion steps. In the crimping step (Fig. 5, panel (A)), the crimping cylinder is compressed by imposing a radial displacement so that the diameter is reduced from 7.5 mm

to 2.3 mm (corresponding to a catheter of 7 Fr), whereas in the expansion step (Fig. 5, panel (B)) the crimping cylinder is released to the initial diameter. The nodes on the left boundary section of the stent are constrained along the axial direction  $z$ , the boundary nodes along the cylindrical surface undergo the radial compression and expansion of the catheter, while the remaining nodes are left free. Contact between the stent and the crimping cylinder, and self-contacts between the stent struts are modeled with a pure master–slave algorithm, by assuming a friction coefficient of 0.1 and a hard-contact pressure–overclosure relationship [75]. Finally, artificial damping is added to stabilize the nonlinear simulations, in order to control that the ratio between the related dissipation energy and the total internal energy is less than 5%.

To evaluate the structural performance of the new stents, we refer to the design requirements listed in the introduction of Section 2, by considering the following FE outputs:

- the peak maximum principal strain of the stent. With reference to the limit value, the material elongation at break is set to 18%, in accordance with previously conducted tensile tests on NiTi specimens [76];
- the normalized radial force, which is computed as the sum of the generated contact normal forces along the radial direction divided by the initial stent length;
- the normalized stent foreshortening, which is computed as  $(l - l_0)/l_0$ , where  $l_0$  and  $l$  are the initial stent length and the stent length in correspondence with the variable crimping diameter, respectively.

In order to avoid undesirable boundary effects, the FE outputs are computed by considering only the central stent cells as highlighted in Fig. 4, panel (D).

#### 2.4. Hemodynamic features of the stent

As a last step in the workflow in Fig. 1, we investigate the impact of the new stents on the arterial hemodynamics, by performing transient, laminar CFD simulations on the stent designs successfully tested by the FE structural analysis in the previous section. In detail, we place the new devices in an idealized (cylindrical) geometry, modeling the superficial femoral artery with a diameter of 6 mm. To avoid boundary effects, a stent portion approximately 13 mm long, located at 2 and 5 diameters from the model inlet and outlet section, respectively, is here considered.

The stented arterial geometry is discretized using Fluent Meshing (Ansys Inc., Canonsburg, PA, USA). According to [77,36], the fluid domain is discretized with tetrahedral elements in the bulk flow and with five layers of high-quality prismatic cells near the luminal surface. The computational mesh is refined close to the stent struts to sharply detect the small-scale flow features between struts regions (we refer to [36] for a sensitivity analysis of the mesh with respect to the element size).

The finite volume-based commercial code Fluent is adopted to numerically solve the discretized unsteady Navier–Stokes equations, by assuming the blood as an incompressible, homogeneous fluid, with constant density equal to  $1060 \text{ kg m}^{-3}$ . The shear-thinning blood behavior is modeled using the non-Newtonian Carreau model, describing the relationship between viscosity and shear rate  $\dot{\gamma}$  as follows:

$$\mu(\dot{\gamma}) = \mu_\infty + (\mu_0 - \mu_\infty)[1 + (\mathcal{T}\dot{\gamma})^2]^{\frac{m-1}{2}}, \quad (24)$$

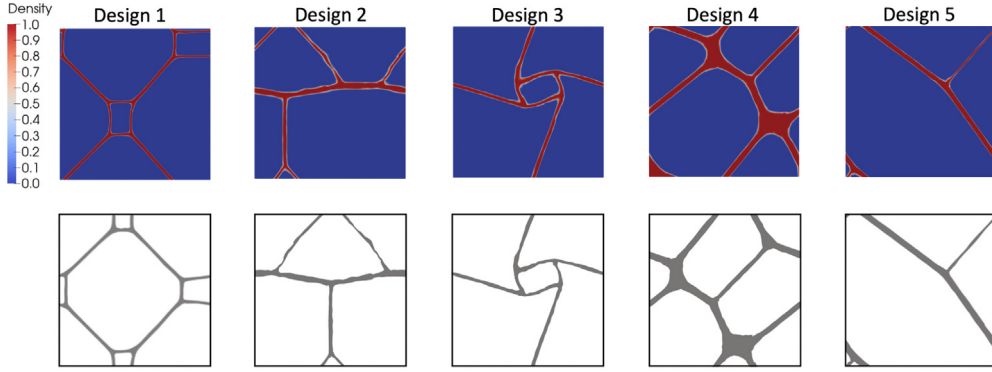
where  $\mu_\infty = 0.0035 \text{ Pa s}$  and  $\mu_0 = 0.25 \text{ Pa s}$  are the infinite and zero shear rate limit viscosities, respectively,  $\mathcal{T} = 25 \text{ s}$  is the relaxation time constant, and  $m = 0.25$  is the power law index [78]. Concerning the boundary conditions, at the inlet section we prescribe a patient-specific parabolic velocity profile, derived from Doppler ultrasound images [36]. In detail, the pulsatile inflow waveform amplitude is scaled with respect to the inlet diameter to ensure a physiological mean flow rate value. A reference pressure is imposed at the outflow section. The no-slip condition is applied to the vessel and stent walls, here assumed as rigid. Further details on the numerical setting are exhaustively provided in [36].

The hemodynamic characteristics of the stent design are evaluated according to the fourth design requirement listed in the introduction of Section 2. In detail, the local hemodynamics along the stented region is analyzed in terms of the canonical quantity TAWSS (Time-Averaged Wall Shear Stress), namely the average WSS magnitude value along the cardiac cycle. In addition, we investigate the WSS topological skeleton features at the stented region, due to the recently emerged link to atherogenesis [79]. Following a recently proposed Eulerian-based approach [80], the divergence of the normalized WSS vector field,  $\sigma_{\text{WSS}}$ , is used to identify the WSS contraction and expansion

**Table 2**

Designs 1–5. MicroSIMPATY parameters distinguishing the optimized unit cells.

	$\bar{E}_{1111}$	$\bar{E}_{1111}$	$\bar{E}_{1122}$	$\bar{E}_{1122}$	$r_f$
Design 1	0.25	1.00	0.50	1.00	0.060
Design 2	0.60	0.75	0.15	0.25	0.025
Design 3	0.25	1.00	−0.40	−0.20	0.050
Design 4	0.50	1.00	0.75	1.25	0.075
Design 5	0.25	0.80	0.50	0.90	0.060

**Fig. 6.** Optimized unit cells  $\tau$  (top) and associated .stl geometries (bottom) for Designs 1–5 (left–right).

areas at the stented vessel surface. Then, the amount of variation in WSS contraction/expansion action along the cardiac cycle  $[0, T]$  is quantified by the Topological Shear Variation Index (TSVI), with

$$\text{TSVI} = \left[ \frac{1}{T} \int_0^T [\nabla \cdot \sigma_{\text{WSS}} - \overline{\nabla \cdot \sigma_{\text{WSS}}}]^2 dt \right]^{1/2}, \quad (25)$$

namely the root-mean-square deviation of the divergence of  $\sigma_{\text{WSS}}$  with respect to the associated spatial average [81,79,82].

### 3. Results

In this section, we consider five proof-of-concept stent designs and analyze the associated structural and fluid dynamics performance.

#### 3.1. TO-based stent unit cell designs

We employ Algorithm 1 for the design of four new stent unit cells, in addition to Design 1 in Section 2.1. The optimization phase essentially preserves the selected functional, the material properties, and the input parameters to microSIMPATY as for Design 1, except for the lower and upper bounds of the components of the stiffness tensor ( $\underline{e}_c, \bar{e}_c$ ) in (11), and for the starting radius  $r_f$  of the Helmholtz filter, differently set for each design as summarized in Table 2. We remark that the constrained stiffness tensor components chosen to drive this analysis are meant to modulate the stent stiffness along one of the main directions and to possibly favor the auxetic behavior of the unit cells, in accordance with [28]. In detail, Design 2 is the output of the optimization when microSIMPATY is applied to narrow intervals for  $E_{1111, \rho_h}^H$  and  $E_{1122, \rho_h}^H$ ; Design 3 is the output when imposing negative values of  $E_{1122, \rho_h}^H$  in the optimization strategy, with a view to an auxetic stent design; Designs 4 and 5 are considered to investigate the sensitivity of the final layout with respect to the range for  $E_{1111, \rho_h}^H$  and  $E_{1122, \rho_h}^H$ .

The optimized densities  $\tau$  delivered by microSIMPATY for the five parameter settings are shown in Fig. 6, together with the associated geometries (where the clear-cut designs  $\tau$  are repositioned and converted into the .stl format). From this figure, the heterogeneity of the stent cells is evident. The originality of the optimized layouts stands out when compared with common designs currently employed in the production of commercial stents [3].

**Table 3**

Designs 1–5. Volume fraction characterizing the final microSIMPATY layout.

	Volume fraction (%)
Design 1	6.11
Design 2	7.52
Design 3	6.55
Design 4	16.55
Design 5	5.56

By visual inspection, it turns out that: Designs 2 and 3 exhibit thinner connection struts, essentially aligned with the horizontal and vertical directions; Designs 4 and 5 generate more closely connected structures and are more similar to Design 1, by offering a diagonal rotation and stretching of the cell unit of the latter.

Some quantitative comments on the output of microSIMPATY are in order. We first consider the converged objective functional, namely the minimization of the contact area between the stent and the arterial walls, expressed in terms of material volume fraction (see Table 3). The final layouts feature a 5.6%–7.5% volume fraction of the initial design domain, consistently with the very thin struts characterizing the designs in Fig. 6. In these cases, the significant minimization of  $J_S$  can be ascribed to the wide ranges selected for the constraints. Conversely, Design 4 represents an exception, with a final 16.55% volume fraction, which is promoted by the larger values enforced for  $E_{1122,\rho_h}^H$  (see Table 2). As a general consideration, we remark that the values achieved for the volume fraction are similar to or even lower than the ones characterizing the stents available on the market.

As a last check, we provide the homogenized stiffness tensor for the cells, given by (23) for Design 1 and

$$\mathbf{E}_\tau^H = \begin{pmatrix} 0.600 & 0.151 & -0.002 \\ 0.151 & 0.099 & 0.0003 \\ -0.002 & 0.0003 & 0.009 \end{pmatrix} \quad \text{for Design 2,}$$

$$\mathbf{E}_\tau^H = \begin{pmatrix} 0.289 & -0.200 & -0.077 \\ -0.200 & 0.196 & 0.066 \\ -0.077 & 0.066 & 0.025 \end{pmatrix} \quad \text{for Design 3,}$$

$$\mathbf{E}_\tau^H = \begin{pmatrix} 0.824 & 0.772 & 0.066 \\ 0.772 & 0.848 & 0.057 \\ 0.066 & 0.057 & 0.368 \end{pmatrix} \quad \text{for Design 4,}$$

$$\mathbf{E}_\tau^H = \begin{pmatrix} 0.510 & 0.519 & -0.376 \\ 0.519 & 0.539 & -0.384 \\ -0.376 & -0.384 & 0.298 \end{pmatrix} \quad \text{for Design 5.}$$

The optimized values  $E_{1111,\tau}^H$  and  $E_{1122,\tau}^H$  are compliant with the lower and upper bounds summarized in Table 2 for all the design cases. It is worth noticing that  $E_{1122,\tau}^H$  is just above the lower bound for Designs 1, 2, 4, 5 and just below the upper bound in the case of Design 3. This can be justified since the optimization process reduces the volume fraction at the expense of stiffness, within the allowed ranges for the constrained components. This trend is less evident for  $E_{1111,\tau}^H$  due to the wider range of admissible values.

### 3.2. Structural mechanics simulations

In this section, we carry out the FE structural analysis set in Section 2.3 on the 3D stent models associated with the 2D unit cells in Fig. 6. Virtual crimping is adopted to discriminate among the five stent layouts. For each stent model, the distributions of the maximum principal strain at the initial and at the minimum crimping diameter are presented in Fig. 7 (we refer also to Table 4 for corresponding quantitative data).

From virtual crimping, we observe that: Design 2 is subject to severe buckling instability issues which do not allow for complete stent crimping (Fig. 7, panel (B)); Design 3 exhibits several auto-contacts between the stent struts at the beginning of the crimping, that prevent a further reduction of the catheter diameter and ultimately impede the finalization of the crimping procedure (Fig. 7, panel (C)); Design 4 reports structural integrity issues,

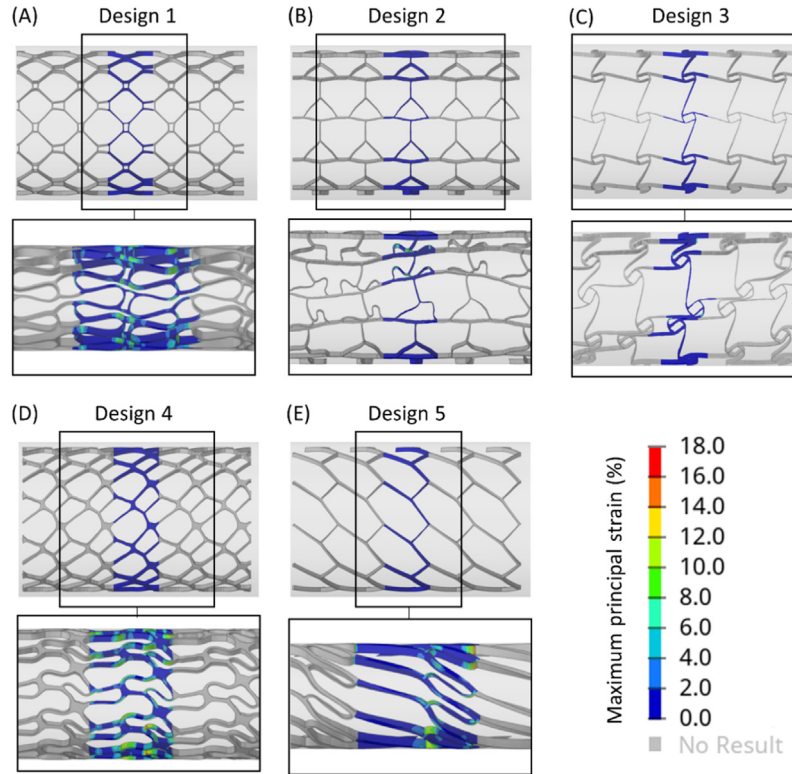


**Fig. 7.** Designs 1–5. Maximum principal strain at the initial (top) and at minimum (bottom) crimping diameter. Half stent of each design is represented in section.

**Table 4**

Designs 1–5. Minimum crimping diameter and corresponding peak value of the maximum principal strain.

	Min crimping diameter (mm)	Peak max principal strain (%)
Design 1	2.3	10.0
Design 2	5.4	12.7
Design 3	5.3	11.1
Design 4	4.0	18.0
Design 5	2.3	15.0

with a peak of maximum principal strain larger than the value of elongation at break. On the contrary, it turns out that Designs 1 and 5 can be adequately crimped. In particular, with reference to [Table 4](#), Designs 1 and 5 allow reaching the target minimum catheter diameter, 2.3 mm, whereas the other three devices fail. Moreover, Design 1 is characterized by the lowest overall value of the peak maximum principal strain and, consequently, it has the lowest risk for structural failure throughout the device deployment procedure [18].

As a second level of investigation, radial force and foreshortening as a function of the crimping diameter are analyzed (see [Fig. 8](#)). A nonlinear trend shows up, to be ascribed to the combined effect of the material super-elasticity and buckling instabilities. Designs 1 and 5, namely the only stents that complete the crimping step, exhibit a hysteresis cycle as it typically occurs in self-expandable NiTi devices. By analyzing [Fig. 8](#) (panel (A)), we remark that Designs 4 and 5 attain the highest and the lowest values of the radial force at the beginning of the crimping step, respectively. Interestingly, Design 1 and 5 show near constant values of the radial force for the range of crimping diameters equal to [5.5 mm, 2.3 mm] and [6 mm, 4 mm], respectively. In panel (B), we can appreciate that Designs 1, 4 and 5 exhibit near equal foreshortening values at the beginning of the crimping step, whereas Design 2 presents

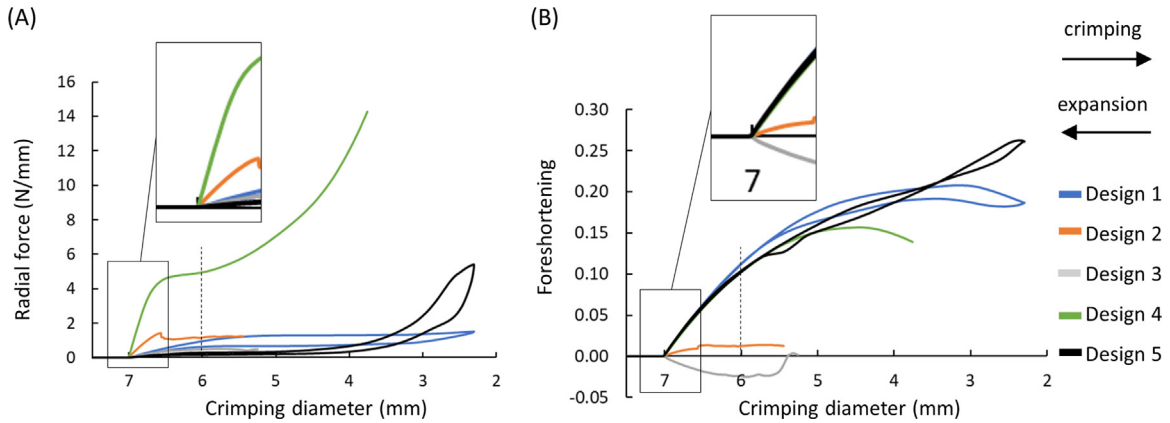


**Fig. 8.** Designs 1–5. Normalized radial force (A) and foreshortening (B) as a function of the crimping diameter. Details are shown for the initial part of the curves. The dotted line marks the intersection between the stent and a vessel with a constant diameter of 6 mm, throughout the expansion step.

**Table 5**

Designs 1 and 5. Normalized radial force and foreshortening values at the crimping diameter of 6 mm in the expansion step.

	Radial force (N/mm)	Foreshortening
Design 1	0.65	0.112
Design 5	0.17	0.105

much lower values. Design 3 takes negative values with an inversion of the trend at the beginning of the crimping step, behaving as an auxetic structure.

Finally, the radial force and the foreshortening values at the diameter of 6 mm during virtual stent expansion are presented in Table 5. We here consider only Designs 1 and 5 since they complete the entire crimping cycle. Markedly different radial force characterizes the two designs.

### 3.3. CFD simulations

Based on the results of the structural analysis, Designs 1 and 5 emerge as potential candidates for innovative stent design. For this reason, CFD simulations for the evaluation of the hemodynamic performance of the stent models are confined to the devices built on Designs 1 and 5 only. The hemodynamic performance is evaluated in terms of the WSS-based quantities introduced in Section 2.4, namely TAWSS and TSVI, whose luminal distributions are mapped over the stented region in Fig. 9. The two designs exhibit similar TAWSS distributions (Fig. 9, top, panels (A) and (B)), with low values localized around the stent struts, and high values located in regions between the struts (i.e., in the stent unit cell central area). Moreover, both stent models present the highest TAWSS in the proximal segment, where an open cell configuration characterizes the stents ring. As for the TSVI luminal distribution, high variations in the WSS contraction/expansion action along the cardiac cycle are mainly located proximal and distal to the stent struts, according to previous observations in commercially available stents (Fig. 9, bottom, panels (A) and (B)) [77]. In both stent models, the highest TSVI values ( $> 5000 \text{ m}^{-1}$ ) are located at the stent peaks and valleys, and at the links between the stent rings. Conversely, lower TSVI values characterize the central region of stent unit cells. Overall, a co-localization between low TAWSS and high TSVI values in the proximity of the stent struts is observable in both stent models.

Despite the observed similarities in TAWSS and TSVI luminal distributions, the extension of the luminal surface regions exposed to low TAWSS and high TSVI values is larger in the stent model based on Design 1. This is confirmed by the quantitative analysis of the distributions of TAWSS and TSVI on the luminal surface region around a single stent ring (see violin plots in Fig. 9, panel (C)). In particular, the stent ring associated with Design

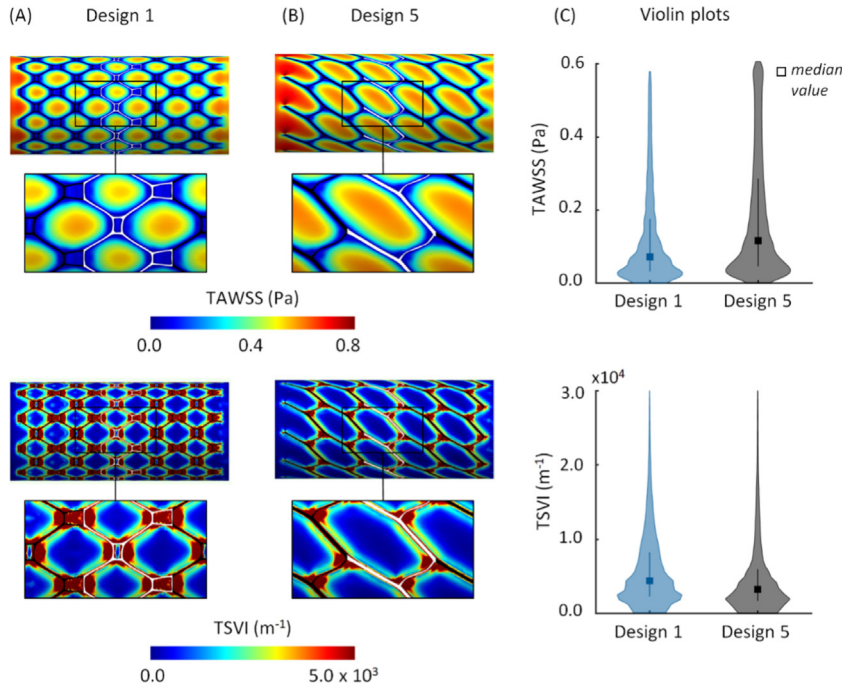


**Fig. 9.** Color maps of TAWSS (top) and TSVI (bottom) along the luminal surface of stented region of Design 1 (A) and Design 5 (B). Violin plots (C) of TAWSS (top) and TSVI (bottom) for a single stent ring (white-highlighted in (A) and (B)).

1 presents lower TAWSS and higher TSVI median values as compared to the model corresponding to Design 5 (0.07 [0.03–0.17] Pa versus 0.12 [0.05–0.29] Pa, and 4408 [2359–8237]  $\text{m}^{-1}$  versus 3290 [1750–5987]  $\text{m}^{-1}$ , respectively).

#### 4. Discussion

In the following, we critically examine the results of the proposed TO-based strategy for peripheral stents design, with a view to a possible practical employment and to future enhancements of the workflow.

##### 4.1. Innovation onto the state of the art

The inverse homogenization TO-based computational framework in Section 2.1 offers a disruptive workflow. In the first step of the process, microSIMPATY algorithm is employed to systematically yield unconventional unit cells, instrumental to the design of new self-expandable femoral stents (second step). Compared with the contributions in the literature [26,27] where TO drives the proposal of new stent designs, the approach here introduced resorts to inverse homogenization to efficiently deal with the interplay between the unit cell prototyping and the properties of the whole device. In addition, the process turns out to be general, going beyond the design of auxetic stents as addressed in [28,29]. A further innovative feature characterizing the new pipeline is represented by the employment of computational meshes highly customized to the TO process. This peculiarity makes the whole design process time- and cost-effective, and promotes completely original layouts.

In the last two steps of the workflow, a verification is accomplished to determine the biomechanical performance guaranteed by the new stent designs, focusing on the actual geometric, structural and hemodynamic properties. In particular, the new workflow also takes into account the minimum requirement for usability, by simulating the device crimping up to the catheter diameter.

#### 4.2. New stent designs: The topology optimization process

The considerable versatility of the new design process is confirmed by the high heterogeneity exhibited by the proof-of-concept layouts in Section 3.1, in terms of both topology and mechanical/hemodynamic performance (see Sections 3.2 and 3.3). This variety of solutions is unlocked by the different choices for the objective functional and for the constraints of the optimization problem (11), as well as by the numerical parameters involved in Algorithm 1 (see, e.g., [69,49]). In this context, a key role is played by the selected ranges for the homogenized stiffness tensor components, promoting the proposal of unit cells with an original layout when compared with the ones commonly employed in the stent production. From a mathematical viewpoint, the heterogeneity of the topologically optimized layout can be ascribed to the non-convexity of problem (11), namely to the existence of several local minima [25]. Moreover, the adoption of an anisotropic mesh adaptation in the design process leads to fully sustainable computations. For instance, the prototyping of a new stent unit cell requires, on average, 15 minutes on a standard laptop.

In more detail, the analysis carried out in Section 3.1 highlights that large values for the homogenized stiffness tensor components promote high volume fractions (i.e., a high contact area), while wide ranges for the constraints lead to a relevant reduction of the volume fraction (i.e., a low contact area). The obtained volume fractions are in the range 5–7% (except for Design 4 with 16.55%), which are smaller with respect to those of some commercially available femoral stents, such as the EverFlex stent (EV3, Medtronic, Dublin, Ireland), characterized by a volume fraction of around 18%.

Concerning the homogenized stiffness tensor components, we remark that the optimization procedure reduces the volume fraction at the expense of the stiffness.

To summarize, all the considerations above have to be taken into account in a realistic modeling of new stents in order to match the recommended pre-clinical assessment targets.

#### 4.3. New stent designs: Structural mechanics and CFD analysis

The FE analysis suggests that only Designs 1 and 5 meet the minimum requirements for usability throughout the implantation procedure, in terms of device crimpability into the catheter. When compared to Design 5, Design 1 exhibits: a lower value of the peak maximum principal strain at the catheter diameter, i.e., a higher safety in terms of structural integrity, with reference to the material elongation at break limit; a higher radial force; a similar foreshortening at the implantation diameter (see Table 5).

More in detail, despite the regulatory documentation [38,37] does not enforce limit values, the radial force should not be too low, to avoid incomplete apposition of the stent to the vessel wall, nor excessive, to limit injuring of the surrounding tissue; the foreshortening should be ideally as close as possible to zero, to precisely implant the device into the vessel [3]. In [83], the authors experimentally evaluated the radial force generated by three commercially available self-expandable peripheral stents, when considering a radial compression of 1 mm in diameter, establishing that such a force is expected to be in the range [0.4 N/mm, 1 N/mm]. The radial force of Designs 1 and 5, at the same diameter of radial compression, are equal to 0.65 N/mm and 0.17 N/mm, respectively (Table 4). Accordingly, the radial force generated by Design 1 is within the admissible range, whereas Design 5 features a force value out of the range.

With reference to hemodynamics, Design 1, which is characterized by a slightly higher volume fraction, exhibits lower TAWSS and higher TSVI median values than Design 5 (Fig. 9). It follows that Design 1 may be subject to a higher risk of ISR [77,34,84,85].

Summarizing, the findings of the structural mechanics and fluid dynamics analyses suggest that Design 1 performs better in terms of mechanical characteristics (i.e., lower peak maximum principal strain, radial force in the range of commercial devices), while Design 5 is better in terms of geometric (i.e., lower contact area) and hemodynamics characteristics. Further investigation is required to define the best stent design, through the execution of other *in silico* tests (e.g., crush and kink tests) and the fabrication of real prototypes for a final *in vitro* assessment.

#### 4.4. Current limits and future perspectives

The proposed workflow proved to be a reliable computational tool to generate innovative stents that ensure adequate performances in terms of usability, radial force and hemodynamics, although limited to a specific setting

of design and validation criteria. In particular, the choice for the selected components of the homogenized stiffness tensor and for the associated range of variation in Section 3 has to be meant just as a possible design instance, that allows us to tune the stent stiffness along one of the main directions and, possibly, to promote the auxetic behavior of the unit cells, in accordance with [28]. Concerning the validation, the mechanical performance of the stents has been assessed by simulating the radial crimping only, since it represents the most relevant loading condition that the stent undergoes through the implantation procedure.

It is worth noticing that the proposed design workflow is flexible and modular. This property unlocks the possibility to endow the design and verification phases with diversified requirements and a posteriori tests. It could be of interest to constrain other stiffness tensor components, for instance to model a multi-axial loading or to impose an isotropic mechanical response. As for the mechanical tests, we plan to assess complex loading scenarios in femoropopliteal arteries, such as bending, torsion, axial compression and tension, and pinching, related to the lower limb movements [31,32].

In order to broaden the range of applications, the potentiality of the current workflow could be further enhanced by introducing more massive modifications to the problem setting in (11). As a possible, although very challenging, improvement, we plan to include the requirements currently employed to a posteriori assess the biomechanical behavior of new stent devices into the optimization problem (11), for instance as additional constraints or by modifying the goal functional. With this regard, a multiphysics TO-based approach could be developed, thus driving the optimization by means of both structural mechanics and fluid dynamics requirements. Also, it would be of interest to incorporate as parameters of the optimization process the strut thickness and the number of circumferential repetitions of the stent [86,87], which are maintained fixed at this stage of the study.

In view of industry-driven applications, possible improvements relate to: the introduction of manufacturability constraints and of CAD-compatible discretizations [88,89] in the design of 2D stent unit cells; the choice of the selected alloy, in order to take into account the dependence of the NiTi material properties on the chemical composition and on the thermo-mechanical processing operations [90]; the extension of the proposed pipeline to the design of medical devices for other cardiovascular applications or in different medical areas (we refer to [50] for an instance of orthopedic application).

## 5. Conclusions

In the last decade the technological innovation in femoral artery stenting has been incremental, with minimal modifications to the geometry of consolidated stent designs, resulting in marginal improvements in stents performance. Such an incremental approach considerably limits the proposal of innovative devices on the market. On the contrary, the computational workflow here presented enables the creation of breakthrough designs of self-expandable femoral artery stents, thanks to the employment of inverse homogenization TO for the generation of new stent unit cells that meet specific design requirements. Five proof-of-concept stent layouts with different topologies were successfully generated and *in silico* verifications were carried out to assess the associated mechanical and hemodynamic performance. Two of the identified stent designs exhibited promising results in terms of stent usability throughout the implantation procedure, low values for the surface contact area and adequate radial force.

Overall, the method has to be meant as a proof-of-concept to assess the capability of the workflow in Fig. 1 to match a set of specific requirements for the stent design. The versatility of the involved methodology guarantees the generalization of the whole process to different objectives, up to a patient-specific setting.

## Declaration of competing interest

The authors declare that they have no known competing financial interests or personal relationships that could have appeared to influence the work reported in this paper.

## Data availability

No data was used for the research described in the article.

## Acknowledgments

NF and SP thank the PRIN research grant n. 20204LN5N5 *Advanced Polyhedral Discretisations of Heterogeneous PDEs for Multiphysics Problems*. NF and SP acknowledge the support by MUR, grant Dipartimento di Eccellenza 2023–2027. NF acknowledges the INdAM–GNCS 2023 Project *Algoritmi efficienti per la gestione e adattamento di mesh poligonali*. CC, DG and UM acknowledge the Italian Ministry of Education, University and Research for the research grant FISR2019 03221 *CECOMES*. ALA, CC and DC acknowledge the Piedmont Region, Italy for the research grant POR FESR PiTeF 2014–20 351-96 *Nitiliera*. FM acknowledges the support of the FARD-2023 research funds from the Department of Engineering “Enzo Ferrari”, University of Modena and Reggio Emilia.

## References

- [1] M. Hejazi, F. Sassani, J. Gagnon, Y. Hsiang, A.S. Phani, Deformation mechanics of self-expanding venous stents: Modelling and experiments, *J. Biomech.* 120 (2021) 110333, <http://dx.doi.org/10.1016/j.jbiomech.2021.110333>, [arXiv:2102.10219](https://arxiv.org/abs/2102.10219).
- [2] W. Jiang, W. Zhao, T. Zhou, L. Wang, T. Qiu, A review on manufacturing and post-processing technology of vascular stents, *Micromachines* 13 (1) (2022) 140, <http://dx.doi.org/10.3390/mi13010140>.
- [3] C. Pan, Y. Han, J. Lu, Structural design of vascular stents: A review, *Micromachines* 12 (7) (2021) 770, <http://dx.doi.org/10.3390/mi12070770>.
- [4] B. Polanec, J. Kramberger, S. Glodež, A review of production technologies and materials for manufacturing of cardiovascular stents, *Adv. Prod. Eng. Manag.* 15 (4) (2020) 390–402, <http://dx.doi.org/10.14743/APEM2020.4.373>.
- [5] T.W. Duerig, M. Wholey, A comparison of balloon- and self-expanding stents, *Minim. Invasive Ther. Allied Technol.* 11 (4) (2002) 173–178, <http://dx.doi.org/10.1080/136457002760273386>.
- [6] T. Schmidt, J.D. Abbott, Coronary stents: History, design, and construction, *J. Clin. Med.* 7 (6) (2018) 126, <http://dx.doi.org/10.3390/jcm7060126>.
- [7] W. Kim, D. Choi, Treatment of femoropopliteal artery in-stent restenosis, *Korean Circ. J.* 48 (3) (2018) 191–197, <http://dx.doi.org/10.4070/kcj.2018.0074>.
- [8] E. Shlofmitz, M. Iantorno, R. Waksman, Restenosis of drug-eluting stents: A new classification system based on disease mechanism to guide treatment and state-of-the-art review, *Circ. Cardiovasc. Inter.* 12 (8) (2019) e007023, <http://dx.doi.org/10.1161/CIRCINTERVENTIONS.118.007023>.
- [9] B. Tomberli, A. Mattesini, G.I. Baldereschi, C. Di Mario, A brief history of coronary artery stents, *Rev. Esp. Cardiol.* 71 (5) (2018) 312–319, <http://dx.doi.org/10.1016/j.recresp.2017.11.016>.
- [10] A.K. Kareem, M.M. Gabir, I.R. Ali, A.E. Ismail, I. Taib, N. Darlis, O.M. Almoayed, A review on femoropopliteal arterial deformation during daily lives and nickel-titanium stent properties, *J. Med. Eng. Technol.* 46 (4) (2022) 300–317, <http://dx.doi.org/10.1080/03091902.2022.2041749>.
- [11] A. Qiao, Z. Zhang, Numerical simulation of vertebral artery stenosis treated with different stents, *J. Biomech. Eng.* 136 (4) (2014) 041007, <http://dx.doi.org/10.1115/1.4026229>.
- [12] R.A. Byrne, M. Joner, A. Kastrati, Stent thrombosis and restenosis: What have we learned and where are we going? The Andreas Grüntzig lecture ESC 2014, *Eur. Heart J.* 36 (47) (2015) 3320–3331, <http://dx.doi.org/10.1093/eurheartj/ehv511>.
- [13] R. Reejhsinghani, A.S. Lotfi, Prevention of stent thrombosis: Challenges and solutions, *Vasc. Health Risk Manage.* 11 (2015) 93–106, <http://dx.doi.org/10.2147/VHRM.S43357>.
- [14] T.M. Morrison, M.L. Dreher, S. Nagaraja, L.M. Angelone, W. Kainz, The role of computational modeling and simulation in the total product life cycle of peripheral vascular devices, *J. Med. Devices* 11 (2) (2017) 024503, <http://dx.doi.org/10.1115/1.4035866>.
- [15] T.M. Morrison, P. Pathmanathan, M. Adwan, E. Margerrison, Advancing regulatory science with computational modeling for medical devices at the FDA’s office of science and engineering laboratories, *Front. Med.* 5 (2018) 241, <http://dx.doi.org/10.3389/fmed.2018.00241>.
- [16] G. Alaimo, F. Auricchio, M. Conti, M. Zingales, Multi-objective optimization of nitinol stent design, *Med. Eng. Phys.* 47 (2017) 13–24, <http://dx.doi.org/10.1016/j.medengphy.2017.06.026>.
- [17] R. Clune, D. Kelliher, J.C. Robinson, J.S. Campbell, NURBS modeling and structural shape optimization of cardiovascular stents, *Struct. Multidiscip. Optim.* 50 (1) (2014) 159–168, <http://dx.doi.org/10.1007/s00158-013-1038-y>.
- [18] E. Masoumi Khalil Abad, D. Pasini, R. Cecere, Shape optimization of stress concentration-free lattice for self-expandable Nitinol stent-grafts, *J. Biomech.* 45 (6) (2012) 1028–1035, <http://dx.doi.org/10.1016/j.jbiomech.2012.01.002>.
- [19] S. Pant, G. Limbert, N.P. Curzen, N.W. Bressloff, Multiobjective design optimisation of coronary stents, *Biomaterials* 32 (31) (2011) 7755–7773, <http://dx.doi.org/10.1016/j.biomaterials.2011.07.059>.
- [20] S. Pant, N.W. Bressloff, G. Limbert, Geometry parameterization and multidisciplinary constrained optimization of coronary stents, *Biomech. Model. Mechanobiol.* 11 (1–2) (2012) 61–82, <http://dx.doi.org/10.1007/s10237-011-0293-3>.
- [21] N.S. Ribeiro, J. Folgado, H.C. Rodrigues, Surrogate-based multi-objective design optimization of a coronary stent: Altering geometry toward improved biomechanical performance, *Int. J. Numer. Method. Biomed. Eng.* 37 (6) (2021) e3453, <http://dx.doi.org/10.1002/cnm.3453>.
- [22] W. Wu, L. Petrini, D. Gastaldi, T. Villa, M. Vedani, E. Lesma, B. Previtali, F. Migliavacca, Finite element shape optimization for biodegradable magnesium alloy stents, *Ann. Biomed. Eng.* 38 (9) (2010) 2829–2840, <http://dx.doi.org/10.1007/s10439-010-0057-8>.
- [23] M.M. Torki, S. Hassanajili, M.M. Jalisi, Design optimizations of PLA stent structure by FEM and investigating its function in a simulated plaque artery, *Math. Comput. Simulation* 169 (2020) 103–116, <http://dx.doi.org/10.1016/j.matcom.2019.09.011>.

- [24] S. Čanić, L. Grubišić, D. Lacmanović, M. Ljulj, J. Tambača, Optimal design of vascular stents using a network of 1D slender curved rods, *Comput. Methods Appl. Mech. Engrg.* 394 (2022) 114853, <http://dx.doi.org/10.1016/j.cma.2022.114853>.
- [25] M.P. Bendsøe, O. Sigmund, *Topology Optimization: Theory, Methods and Applications*, second ed., Springer, 2004.
- [26] W. Wu, D.Z. Yang, Y.Y. Huang, M. Qi, W.Q. Wang, Topology optimization of a novel stent platform with drug reservoirs, *Med. Eng. Phys.* 30 (9) (2008) 1177–1185, <http://dx.doi.org/10.1016/j.medengphy.2008.02.010>.
- [27] K.A. James, H. Waisman, Layout design of a bi-stable cardiovascular stent using topology optimization, *Comput. Methods Appl. Mech. Engrg.* 305 (2016) 869–890, <http://dx.doi.org/10.1016/j.cma.2016.02.036>.
- [28] H. Xue, Z. Luo, T. Brown, S. Beier, Design of self-expanding auxetic stents using topology optimization, *Front. Bioeng. Biotechnol.* 8 (2020) 736, <http://dx.doi.org/10.3389/fbioe.2020.00736>.
- [29] H. Xue, S.C. Saha, S. Beier, N. Jepson, Z. Luo, Topological optimization of auxetic coronary stents considering hemodynamics, *Front. Bioeng. Biotechnol.* 9 (2021) 728914, <http://dx.doi.org/10.3389/fbioe.2021.728914>.
- [30] H.X. Li, W.L. Shi, Z. Tan, M.J. Wang, D.Y. Zhao, J. Yan, Topology optimization for polymeric stent, *Struct. Multidiscip. Optim.* 65 (7) (2022) 194, <http://dx.doi.org/10.1007/s00158-022-03292-z>.
- [31] C.P. Cheng, N.M. Wilson, R.L. Hallett, R.J. Herfkens, C.A. Taylor, In vivo MR angiographic quantification of axial and twisting deformations of the superficial femoral artery resulting from maximum hip and knee flexion, *J. Vasc. Interv. Radiol.* 17 (6) (2006) 979–987, <http://dx.doi.org/10.1097/01.RVI.00000220367.62137.e8>.
- [32] J.N. MacTaggart, N.Y. Phillips, C.S. Lomneth, I.I. Pipinos, R. Bowen, B. Timothy Baxter, J. Johanning, G. Matthew Longo, A.S. Desyatova, M.J. Moulton, Y.A. Dzenis, A.V. Kamenskiy, Three-dimensional bending, torsion and axial compression of the femoropopliteal artery during limb flexion, *J. Biomech.* 47 (10) (2014) 2249–2256, <http://dx.doi.org/10.1016/j.jbiomech.2014.04.053>.
- [33] N. Ferro, S. Micheletti, S. Perotto, Density-based inverse homogenization with anisotropically adapted elements, in: A. Corsini, S. Perotto, G. Rozza, H. van Brummelen (Eds.), *Numerical Methods for Flows*, vol. 132, in: *Lecture Notes in Computational Science and Engineering*, Springer, 2020, pp. 211–221, [http://dx.doi.org/10.1007/978-3-030-30705-9\\_19](http://dx.doi.org/10.1007/978-3-030-30705-9_19).
- [34] K.C. Koskinas, Y.S. Chatzizisis, A.P. Antoniadis, G.D. Giannoglou, Role of endothelial shear stress in stent restenosis and thrombosis: Pathophysiologic mechanisms and implications for clinical translation, *J. Am. Coll. Cardiol.* 59 (15) (2012) 1337–1349, <http://dx.doi.org/10.1016/j.jacc.2011.10.903>.
- [35] D. Károlyi, M. Kovács, A.A. Terdik, E. Bognár, Investigation of metallic surface area of coronary stents, *Biomech. Hung.* 6 (2013) <http://dx.doi.org/10.17489/biohun/2013/1/23>.
- [36] M. Colombo, A. Corti, D. Gallo, A. Colombo, G. Antognoli, M. Bernini, C. McKenna, S. Berceli, T. Vaughan, F. Migliavacca, C. Chiastra, Superficial femoral artery stenting: Impact of stent design and overlapping on the local hemodynamics, *Comput. Biol. Med.* 144 (2022) 105248, <http://dx.doi.org/10.1016/j.compbiomed.2022.105248>.
- [37] ISO, *Cardiovascular Implants — Endovascular Devices — Part 2: vascular Stents*, 2012.
- [38] FDA, *Non-Clinical Engineering Tests and Recommended Labeling for Intravascular Stents and Associated Delivery Systems*, 2010.
- [39] A. Bensoussan, J.L. Lions, G. Papanicolaou, *Asymptotic Analysis for Periodic Structures*, AMS Chelsea Publishing, Providence, RI, 2011.
- [40] O. Sigmund, *Design of Material Structures using Topology Optimization* (Ph.D. thesis), Technical University of Denmark, Lyngby, Denmark, 1994.
- [41] P. Helmwein, Some remarks on the compressed matrix representation of symmetric second-order and fourth-order tensors, *Comput. Methods Appl. Mech. Engrg.* 190 (22–23) (2001) 2753–2770, [http://dx.doi.org/10.1016/S0045-7825\(00\)00263-2](http://dx.doi.org/10.1016/S0045-7825(00)00263-2).
- [42] A. Ern, J.-L. Guermond, *Theory and practice of finite elements*, in: *Applied Mathematical Sciences*, vol. 159, Springer-Verlag, New York, 2004.
- [43] G. Allaire, F. Jouve, A.-M. Toader, Structural optimization using sensitivity analysis and a level-set method, *J. Comput. Phys.* 194 (1) (2004) 363–393.
- [44] M. Bendsøe, O. Sigmund, Material interpolation schemes in topology optimization, *Arch. Appl. Mech.* 69 (1999) 635–654, <http://dx.doi.org/10.1007/s004190050248>.
- [45] O. Sigmund, J. Petersson, Numerical instabilities in topology optimization: A survey on procedures dealing with checkerboards, mesh-dependencies and local minima, *Struct. Optim.* 16 (1) (1998) 68–75, <http://dx.doi.org/10.1007/BF01214002>.
- [46] S. Micheletti, S. Perotto, L. Soli, Topology optimization driven by anisotropic mesh adaptation: Towards a free-form design, *Comput. Struct.* 214 (2019) 60–72, <http://dx.doi.org/10.1016/j.compstruc.2019.01.005>.
- [47] N. Ferro, S. Micheletti, S. Perotto, POD-assisted strategies for structural topology optimization, *Comput. Math. Appl.* 77 (10) (2019) 2804–2820, <http://dx.doi.org/10.1016/j.camwa.2019.01.010>.
- [48] N. Ferro, S. Micheletti, S. Perotto, Compliance–stress constrained mass minimization for topology optimization on anisotropic meshes, *SN Appl. Sci.* 2 (7) (2020) 1–11, <http://dx.doi.org/10.1007/s42452-020-2947-1>.
- [49] D. di Cristofaro, C. Galimberti, D. Bianchi, R. Ferrante, N. Ferro, M. Mannisi, S. Perotto, Adaptive topology optimization for innovative 3D printed metamaterials, in: *Proceedings of WCCM-ECCOMAS 2020 Conference - Modeling and Analysis of Real World and Industry Applications*, vol. 1200, 2021.
- [50] N. Ferro, S. Perotto, D. Bianchi, R. Ferrante, M. Mannisi, Design of cellular materials for multiscale topology optimization: Application to patient-specific orthopedic devices, *Struct. Multidiscip. Optim.* 65 (3) (2022) 79, <http://dx.doi.org/10.1007/s00158-021-03163-z>.
- [51] N. Ferro, S. Perotto, M. Gavazzoni, A new fluid-based strategy for the connection of non-matching lattice materials, *Struct. Multidiscip. Optim.* 65 (10) (2022) 15, <http://dx.doi.org/10.1007/s00158-022-03354-2>, Paper No. 287.
- [52] K.E. Jensen, Solving stress and compliance constrained volume minimization using anisotropic mesh adaptation, the method of moving asymptotes and a global p-norm, *Struct. Multidiscip. Optim.* 54 (4) (2016) 831–841, <http://dx.doi.org/10.1007/s00158-016-1439-9>.
- [53] O.C. Zienkiewicz, J.Z. Zhu, A simple error estimator and adaptive procedure for practical engineering analysis, *Internat. J. Numer. Methods Engrg.* 24 (2) (1987) 337–357, <http://dx.doi.org/10.1002/nme.1620240206>.

- [54] O.C. Zienkiewicz, J.Z. Zhu, The superconvergent patch recovery and a posteriori error estimates. Part I. The recovery technique, *Internat. J. Numer. Methods Engrg.* 33 (7) (1992) 1331–1364, <http://dx.doi.org/10.1002/nme.1620330702>.
- [55] R. Rodríguez, Some remarks on Zienkiewicz-Zhu estimator, *Numer. Methods Partial Differential Equations* 10 (5) (1994) 625–635, <http://dx.doi.org/10.1002/num.1690100509>.
- [56] C. Carstensen, All first-order averaging techniques for a posteriori finite element error control on unstructured grids are efficient and reliable, *Math. Comp.* 73 (247) (2004) 1153–1165.
- [57] A. Naga, Z. Zhang, A posteriori error estimates based on the polynomial preserving recovery, *SIAM J. Numer. Anal.* 42 (4) (2004) 1780–1800, <http://dx.doi.org/10.1137/S0036142903413002>.
- [58] N. Yan, A. Zhou, Gradient recovery type a posteriori error estimates for finite element approximations on irregular meshes, *Comput. Methods Appl. Mech. Engrg.* 190 (32–33) (2001) 4289–4299, [http://dx.doi.org/10.1016/S0045-7825\(00\)00319-4](http://dx.doi.org/10.1016/S0045-7825(00)00319-4).
- [59] G. Maisano, S. Micheletti, S. Perotto, C.L. Bottasso, On some new recovery-based a posteriori error estimators, *Comput. Methods Appl. Mech. Engrg.* 195 (37–40) (2006) 4794–4815, <http://dx.doi.org/10.1016/j.cma.2005.07.024>.
- [60] S. Micheletti, S. Perotto, Anisotropic adaptation via a Zienkiewicz-Zhu error estimator for 2D elliptic problems, in: G. Kreiss, P. Lötstedt, A. Målqvist, M. Neytcheva (Eds.), *Numerical Mathematics and Advanced Applications*, Springer-Verlag Berlin Heidelberg, 2010, pp. 645–653, [http://dx.doi.org/10.1007/978-3-642-11795-4\\_69](http://dx.doi.org/10.1007/978-3-642-11795-4_69).
- [61] S. Micheletti, S. Perotto, Reliability and efficiency of an anisotropic Zienkiewicz-Zhu error estimator, *Comput. Methods Appl. Mech. Engrg.* 195 (9–12) (2006) 799–835, <http://dx.doi.org/10.1016/j.cma.2005.02.009>.
- [62] F. Hecht, New development in FreeFem++, *J. Numer. Math.* 20 (3–4) (2012) 251–265, <http://dx.doi.org/10.1515/jnum-2012-0013>.
- [63] A. Wächter, L.T. Biegler, On the implementation of an interior-point filter line-search algorithm for large-scale nonlinear programming, *Math. Program.* 1, Ser. A (106) (2006) 25–57, <http://dx.doi.org/10.1007/s10107-004-0559-y>.
- [64] F. Hecht, BAMG: Bidimensional anisotropic mesh generator, 2006, <https://www.ljll.math.upmc.fr/hecht/ftp/bamg/bamg.pdf>.
- [65] S.-W. Cheng, T.K. Dey, J.R. Shewchuk, Delaunay mesh generation, in: *Chapman & Hall/CRC Computer and Information Science Series*, Chapman & Hall/CRC, Boca Raton, FL, 2013.
- [66] N. Ferro, S. Micheletti, S. Perotto, An optimization algorithm for automatic structural design, *Comput. Methods Appl. Mech. Engrg.* 372 (2020) 113335, <http://dx.doi.org/10.1016/j.cma.2020.113335>.
- [67] S. Xu, Y. Cai, G. Cheng, Volume preserving nonlinear density filter based on heaviside functions, *Struct. Multidiscip. Optim.* 41 (2010) 495–505, <http://dx.doi.org/10.1007/s00158-009-0452-7>.
- [68] F. Wang, B.S. Lazarov, O. Sigmund, On projection methods, convergence and robust formulations in topology optimization, *Struct. Multidiscip. Optim.* 43 (2011) 767–784, <http://dx.doi.org/10.1007/s00158-010-0602-y>.
- [69] M. Gavazzoni, N. Ferro, S. Perotto, S. Foletti, Multi-physics inverse homogenization for the design of innovative cellular materials: Application to thermo-elastic problems, *Math. Comput. Appl.* 27 (1) (2022) 15, <http://dx.doi.org/10.3390/mca27010015>.
- [70] C. Capelli, F. Gervaso, L. Petrini, G. Dubini, F. Migliavacca, Assessment of tissue prolapse after balloon-expandable stenting: Influence of stent cell geometry, *Med. Eng. Phys.* 31 (4) (2009) 441–447, <http://dx.doi.org/10.1016/j.medengphy.2008.11.002>.
- [71] C. Chiastra, M.J. Grundeken, C. Collet, W. Wu, J.J. Wykrzykowska, G. Pennati, G. Dubini, F. Migliavacca, Biomechanical impact of wrong positioning of a dedicated stent for coronary bifurcations: A virtual bench testing study, *Cardiovasc. Eng. Technol.* 9 (3) (2018) 415–426, <http://dx.doi.org/10.1007/s13239-018-0359-9>.
- [72] F. Auricchio, R.L. Taylor, J. Lubliner, Shape-memory alloys: Macromodelling and numerical simulations of the superelastic behavior, *Comput. Methods Appl. Mech. Engrg.* 146 (3–4) (1997) 281–312, [http://dx.doi.org/10.1016/S0045-7825\(96\)01232-7](http://dx.doi.org/10.1016/S0045-7825(96)01232-7).
- [73] A. Finotello, R. Gorla, N. Brambilla, F. Bedogni, F. Auricchio, S. Morganti, Finite element analysis of transcatheter aortic valve implantation: Insights on the modelling of self-expandable devices, *J. Mech. Behav. Biomed. Mater.* 123 (June) (2021) 104772, <http://dx.doi.org/10.1016/j.jmbbm.2021.104772>.
- [74] D. Carbonaro, C. Chiastra, U. Morbiducci, A. Audenino, Transcatheter aortic valve with embolic filter: Experiments and simulations, in: *Convegno Nazionale Di Bioingegneria*, 2020, pp. 457–460.
- [75] D. Carbonaro, D. Gallo, U. Morbiducci, A. Audenino, C. Chiastra, In silico biomechanical design of the metal frame of transcatheter aortic valves: Multi-objective shape and cross-sectional size optimization, *Struct. Multidiscip. Optim.* 64 (4) (2021) 1825–1842, <http://dx.doi.org/10.1007/s00158-021-02944-w>.
- [76] L. Petrini, E. Dordoni, D. Allegretti, D. Pott, M. Kitting, F. Migliavacca, G. Pennati, Simplified multistage computational approach to assess the fatigue behavior of a niti transcatheter aortic valve during in vitro tests: A proof-of-concept study, *J. Med. Devices* 11 (2) (2017) 021009, <http://dx.doi.org/10.1115/1.4035791>.
- [77] C. Chiastra, V. Mazzi, M. Lodi Rizzini, K. Calò, A. Corti, A. Acquasanta, G. De Nisco, D. Belligiano, E. Cerrato, D. Gallo, U. Morbiducci, Coronary artery stenting affects wall shear stress topological skeleton, *J. Biomech. Eng.* 144 (6) (2022) 1–11, <http://dx.doi.org/10.1115/1.4053503>.
- [78] C. Chiastra, D. Gallo, P. Tasso, F. Iannaccone, F. Migliavacca, J.J. Wentzel, U. Morbiducci, Healthy and diseased coronary bifurcation geometries influence near-wall and intravascular flow: A computational exploration of the hemodynamic risk, *J. Biomech.* 58 (2017) 79–88, <http://dx.doi.org/10.1016/j.jbiomech.2017.04.016>.
- [79] V. Mazzi, G. De Nisco, A. Hoogendoorn, K. Calò, C. Chiastra, D. Gallo, D.A. Steinman, J.J. Wentzel, U. Morbiducci, Early atherosclerotic changes in coronary arteries are associated with endothelium shear stress contraction/expansion variability, *Ann. Biomed. Eng.* 49 (9) (2021) 2606–2621, <http://dx.doi.org/10.1007/s10439-021-02829-5>.
- [80] V. Mazzi, U. Morbiducci, K. Calò, G. De Nisco, M.L. Rizzini, E. Torta, G.C.A. Caridi, C. Chiastra, D. Gallo, Wall shear stress topological skeleton analysis in cardiovascular flows: Methods and applications, *Mathematics* 9 (7) (2021) 720, <http://dx.doi.org/10.3390/math9070720>.

- [81] G. De Nisco, P. Tasso, K. Calò, V. Mazzi, D. Gallo, F. Condemi, S. Farzaneh, S. Avril, U. Morbiducci, Deciphering ascending thoracic aortic aneurysm hemodynamics in relation to biomechanical properties, *Med. Eng. Phys.* 82 (2020) 119–129, <http://dx.doi.org/10.1016/j.medengphy.2020.07.003>.
- [82] U. Morbiducci, V. Mazzi, M. Domanin, G. De Nisco, C. Vergara, D.A. Steinman, D. Gallo, Wall shear stress topological skeleton independently predicts long-term restenosis after carotid bifurcation endarterectomy, *Ann. Biomed. Eng.* 48 (12) (2020) 2936–2949, <http://dx.doi.org/10.1007/s10439-020-02607-9>.
- [83] T. Matsumoto, Y. Matsubara, Y. Aoyagi, D. Matsuda, J. Okadome, K. Morisaki, K. Inoue, S. Tanaka, T. Ohkusa, Y. Maehara, Radial force measurement of endovascular stents: Influence of stent design and diameter, *Vascular* 24 (2) (2016) 171–176, <http://dx.doi.org/10.1177/1708538115590040>.
- [84] M. Colombo, Y. He, A. Corti, D. Gallo, F. Ninno, S. Casarin, J.M. Rozowsky, F. Migliavacca, S. Berceli, C. Chiastra, In-stent restenosis progression in human superficial femoral arteries: Dynamics of lumen remodeling and impact of local hemodynamics, *Ann. Biomed. Eng.* 49 (9) (2021) 2349–2364, <http://dx.doi.org/10.1007/s10439-021-02776-1>.
- [85] M. Colombo, Y. He, A. Corti, D. Gallo, S. Casarin, J.M. Rozowsky, F. Migliavacca, S. Berceli, C. Chiastra, Baseline local hemodynamics as predictor of lumen remodeling at 1-year follow-up in stented superficial femoral arteries, *Sci. Rep.* 11 (1) (2021) 1613, <http://dx.doi.org/10.1038/s41598-020-80681-8>.
- [86] T.J. Gundert, S.C. Shadden, A.R. Williams, B.K. Koo, J.A. Feinstein, J.F. Ladisa, A rapid and computationally inexpensive method to virtually implant current and next-generation stents into subject-specific computational fluid dynamics models, *Ann. Biomed. Eng.* 39 (5) (2011) 1423–1437, <http://dx.doi.org/10.1007/s10439-010-0238-5>.
- [87] T.J. Gundert, A.L. Marsden, W. Yang, J.F. Ladisa, Optimization of cardiovascular stent design using computational fluid dynamics, *J. Biomech. Eng.* 134 (1) (2012) 011002, <http://dx.doi.org/10.1115/1.4005542>.
- [88] M. Montemurro, T. Roiné, J. Pailhès, Multi-scale design of multi-material lattice structures through a CAD-compatible topology optimisation algorithm, *Eng. Struct.* 273 (2022) 115009, <http://dx.doi.org/10.1016/j.engstruct.2022.115009>.
- [89] M. Montemurro, G. Bertolino, E. Panettieri, Topology optimisation of architected cellular materials from additive manufacturing: Analysis, design, and experiments, *Structures* 47 (2023) 2220–2239, <http://dx.doi.org/10.1016/j.istruc.2022.12.032>.
- [90] D. Carbonaro, S. Zambon, A. Corti, D. Gallo, U. Morbiducci, L. Audenino, C. Chiastra, Impact of nickel – titanium super-elastic material properties on the mechanical performance of self-expandable transcatheter aortic valves, *J. Mech. Behav. Biomed. Mater.* 138 (2023) 105623, <http://dx.doi.org/10.1016/j.jmbbm.2022.105623>.